

# STAR-RIS-Assisted Full-Space Angle Estimation via Finite Rate of Innovation

Ziming Liu, *Member, IEEE*, Tao Chen, *Member, IEEE*, Muran Guo, *Member, IEEE*  
and Francesco Verde, *Senior Member, IEEE*

**Abstract**—Conventional sensor architectures typically restrict angle estimation to the half-space. By enabling simultaneous transmission and reflection, simultaneously transmitting and reflecting reconfigurable intelligent surfaces (STAR-RIS) can support full-space angle detection. This paper develops a full-space angle estimation framework by leveraging a finite rate of innovation (FRI) model enabled by STAR-RIS. We distinguish two practical STAR-RIS configurations: (i) an element-wise uniform setting, where all metasurface elements share identical energy-splitting (ES) coefficients and phase differences, and (ii) a nonuniform ES setting, where the phase difference is common across elements while the ES coefficients vary element-wise to increase design flexibility. For each regime, we formulate the corresponding FRI-based signal model and derive the Ziv–Zakai bound (ZZB) for angle estimation. To recover the underlying FRI sampling structure, we develop a proximal-gradient algorithm implemented via alternating projections in matrix space and establish its convergence. Exploiting the recovered FRI structure, we construct an annihilating filter whose zeros encode user angles, enabling gridless estimation via polynomial root finding. Numerical results demonstrate that the proposed methods operate reliably across both configuration regimes and achieve improved angle estimation performance with low overhead.

**Index Terms**—Finite rate of innovation (FRI), full-space angle estimation, reconfigurable intelligent surface (RIS), simultaneously transmitting and reflecting (STAR) metasurface.

## I. INTRODUCTION

Within integrated sensing and communication (ISAC) systems, direction-of-arrival (DOA) estimation is a core capability underpinning localization, beamforming, and target detection [1], [2]. However, in dense urban environments, obstacles and rich scattering often lead to non-line-of-sight (NLOS) propagation, which can severely degrade DOA accuracy [3]–[5]. Reconfigurable metasurfaces provide a promising architectural solution to mitigate this limitation. In particular, *reconfigurable intelligent surfaces (RISs)* employ tunable elements (e.g., varactor diodes and field-effect transistors) to program the response to incident electromagnetic waves, enabling controllable reflection patterns and improved propagation conditions [6], [7]. Thanks to their ultra-thin profile, low power consumption, and ease of deployment, RISs offer an attractive degree of flexibility compared with conventional sensing front-ends. When strategically placed and jointly optimized with the communication link, RISs can enhance angular sensing robustness and partially compensate NLOS-induced degradation [8], [9].

T. Chen, Z. Liu and M. Guo are with Harbin Engineering University, Harbin, 150001 China (e-mail:chentao@hrbeu.edu.cn, lzmfred@hrbeu.edu.cn and guomuran@hrbeu.edu.cn). F. Verde is with the Department of Engineering, University of Campania Luigi Vanvitelli, Aversa I-81031, Italy (e-mail: francesco.verde@unicampania.it).

Despite these advantages, conventional reflection-only RIS architectures inherently operate over a single hemispherical region ( $0^\circ$  –  $180^\circ$ ). Extending to full-space coverage with reflect-only RIS typically requires multiple panels [10] and careful cooperative calibration or phase alignment across surfaces [11], increasing hardware cost and system complexity. In contrast, *simultaneously transmitting and reflecting RIS (STAR-RIS)* can natively serve users on both sides of a single metasurface. By enabling concurrent transmission and reflection via multi-layer element architectures [12], [13], STAR-RIS removes the hemispherical constraint and makes full-space ( $0^\circ$  –  $360^\circ$ ) localization and sensing [14]–[16].

Recent studies have begun to explore STAR-RIS for ISAC, demonstrating its potential for enhanced geometric coverage and full-space signal manipulation. For example, in multi-user millimeter-wave (mmWave) settings, time-slot switching or mode-coding strategies have been used to separate transmission and reflection domains, enabling cascaded channel estimation under limited pilots and small snapshot budgets [17]. For localization and motion parameter estimation, Fisher information analyses and Cramér–Rao bounds (CRBs) for three-dimensional positioning have been derived, characterizing fundamental performance limits under cooperative uplink-downlink operation [18], [19]. Moreover, sensing-stage estimates of position and velocity, together with delay-Doppler-angle structure in cascaded links, can provide informative priors that improve subsequent communication phases [20], [21]. Standardization efforts have also recognized the importance of STAR-RIS modeling and optimization frameworks, reflecting growing interest in real-time sensing and edge-intelligent deployments [22].

Overall, existing STAR-RIS research establishes a useful foundation for cascaded channel parameter estimation, localization, and ISAC-oriented optimization. Nevertheless, dedicated DOA estimation methods tailored to STAR-RIS remain limited. This gap is significant because STAR-RIS sensing introduces structural features—most notably reflection–transmission coupling and potentially time-varying element responses, which challenge conventional array-processing assumptions and call for low-overhead, full-space angle estimation strategies.

Classical subspace methods, such as MUSIC and ESPRIT [23], [24], rely on multiple snapshots acquired under a fixed array manifold, so that a stable sample covariance reveals orthogonal signal and noise subspaces. In metasurface-aided sensing, each time slot typically applies a distinct global configuration, implying that successive measurements correspond

to different sensing matrices rather than repeated snapshots of the same manifold. As a result, the stationarity needed for covariance-based subspace estimation is violated, and mode-wise covariance construction can incur prohibitive overhead. Sparse reconstruction methods address limited snapshots by exploiting angular-domain sparsity through compressive sensing, using on-grid solvers [25], [26] or off-grid refinements such as sparse Bayesian learning (SBL) [27], [28]. These methods can incorporate time-varying sensing matrices and have therefore been adopted in RIS-assisted settings [29], [30]. However, they typically face a bias-complexity tradeoff: grid discretization induces mismatch errors that require finer or multi-stage grids to mitigate, increasing computational cost [31]. Iterative off-grid refinements reduce bias but add algorithmic overhead and do not directly address the full-space challenge introduced by STAR-RIS coupling.

Gridless super-resolution via atomic norm minimization (ANM) avoids discretization bias and exploits Toeplitz/Hermitian structure for line spectrum recovery. ANM has been investigated in RIS-assisted settings, including uniform linear array (ULA)-based formulations [32], two-dimensional extensions [33], accelerations based on the alternating direction method of multipliers (ADMM) to reduce semidefinite-program (SDP) complexity [33], [34], and robustness to array perturbations [35]. Yet most existing models implicitly assume hemispherical operation and a clean Toeplitz structure. In STAR-RIS systems, reflection-transmission coupling together with *spatially varying (element-wise nonuniform)* STAR-RIS coefficients can distort the Toeplitz/Hermitian structure, making ANM less directly applicable. A recent effort applies ANM to full-space estimation by assuming an *element-wise uniform* STAR-RIS parameterization [36], which underscores the potential of gridless modeling while motivating extensions to practical nonuniform parameter designs.

*Finite-rate-of-innovation (FRI)* methods offer a gridless alternative for line spectral recovery. Similar to ANM, FRI represents the received data as a finite sum of complex exponentials; however, instead of solving a lifted convex program, it exploits algebraic structure through annihilating filters (Prony/moment-based constructions) and polynomial root finding. In STAR-RIS-assisted sensing, the reflected and transmitted observations form a multichannel line-spectrum model, since both components share the same underlying angle-dependent exponentials while undergoing different STAR-RIS-induced weightings. This multichannel structure is compatible with FRI, which can deliver super-resolving capability under limited measurements with moderate computational cost [37]–[40]. Although FRI has been adopted mainly for spectrum estimation [41]–[43], it can be extended to STAR-RIS-enabled ISAC, where sensing matrices vary across slots and full-space angular coverage is required. In particular, FRI avoids grid mismatch, supports low-overhead acquisition, and yields angle estimates directly via polynomial rooting.

#### A. Contributions

In this paper, we adopt the FRI framework to develop DOA estimation methods for full-space users in STAR-RIS-assisted

networks. The main contributions are summarized as follows.

- 1) *Full-space STAR-RIS mapping and regime-dependent FRI modeling:* By exploiting the intrinsic coupling between the STAR-RIS transmission and reflection responses, we establish a full-space mapping between the reflection space (RS) and transmission space (TS). We then consider two practically relevant regimes: (i) an *element-wise uniform* STAR-RIS setting, where all elements share identical energy-splitting (ES) coefficients and phase differences, and (ii) a *nonuniform-ES* setting, where the phase difference is common across elements while the ES coefficients vary element-wise. For each regime, we derive an FRI-based multichannel line-spectrum model suitable for gridless angle recovery.
- 2) *Recovery under the element-wise uniform setting:* For the element-wise uniform case, we show that the resulting sensing model admits a structured (rank-one) form that preserves the desired FRI sampling pattern. We develop an alternating-projection algorithm with an embedded low-rank constraint, implemented via a proximal-gradient scheme to recover denoised FRI samples. The DOA estimates are then obtained by solving the corresponding annihilating-filter equations in a gridless manner.
- 3) *Recovery under nonuniform ES via block-matrix lifting:* When ES coefficients vary across elements, the rank-one structure is generally lost and the effective sensing matrix deviates from the canonical FRI sampling form. To address this, we introduce a single-row block Hankel construction and adapt the alternating-projection framework to the resulting block-matrix structure. We further establish convergence guarantees for the proposed iterative procedure.
- 4) *Performance characterization and validation:* Based on the derived STAR-RIS sensing model, we obtain the Ziv-Zakai bound (ZZB) as a theoretical lower bound on DOA accuracy. Numerical simulations verify the proposed methods across both regimes and demonstrate improved estimation performance with a favorable efficiency-accuracy tradeoff.

#### B. Paper organization

The remainder of this paper is organized as follows. Section II presents the STAR-RIS-assisted system model and the underlying assumptions. Section III develops the proposed FRI-based full-space DOA estimation method under an element-wise uniform STAR-RIS setting. Section IV extends the framework to the nonuniform-ES case and provides the corresponding recovery algorithm with convergence analysis. Section V discusses key design choices and derives the ZZB. Numerical results are reported in Section VI, while Section VII concludes the paper.

## II. SYSTEM MODEL AND BASIC ASSUMPTIONS

We consider an urban uplink communication scenario for user localization, where users are located both outside buildings (outdoor) and inside buildings (indoor). A sensing module equipped with a single radio frequency (RF) sensor at the base

station (BS) collects the uplink signals and estimates the angle information of all the users.<sup>1</sup>

In dense urban deployments, the line-of-sight paths from outdoor users to the BS may be blocked by surrounding buildings, so that only NLOS components are available. For indoor users, building penetration loss and structural blockage further attenuate the direct link, leading to severe degradation of the indoor user-BS channel. To compensate for blockage and simultaneously serve both indoor and outdoor users, a STAR-RIS is mounted on the building facade. The STAR-RIS aggregates uplink signals from all users and steers them toward the BS sensing module. Using the STAR-RIS plane as a reference boundary, the full-space domain is partitioned into two subspaces: the *reflection space* (RS), which lies on the same side as the BS (including outdoor users), and the *transmission space* (TS), which lies on the opposite side (encompassing indoor users). Specifically,  $K_R$  users are located in the RS and  $K_T$  users lie in the TS, resulting in a total of  $K \triangleq K_R + K_T$  users across the full-space domain. We adopt the narrowband signal assumption where the user uplink bandwidth  $\Delta f$  satisfies  $\Delta f \ll f_0$ , with  $f_0$  being the carrier frequency synchronized between the users and STAR-RIS. Moreover, without loss of generality, the STAR-RIS is arranged as a ULA with  $N > K$  elements whose spacing is  $\lambda/2$ , where  $\lambda = c/f_0$  and  $c$  is the speed of light.

Throughout the paper and simulations, we use two angle representations depending on whether a full-space or semi-space convention is adopted. In the full-space representation, the metasurface plane is aligned with the  $0^\circ - 180^\circ$  axis. The surface normal pointing into the RS is defined as  $90^\circ$ , while the normal pointing into the TS is defined as  $270^\circ$ . In the semi-space representation, each subspace is parameterized from  $-90^\circ$  to  $90^\circ$ , where  $0^\circ$  is perpendicular to the metasurface plane in the corresponding subspace. Under this convention, the  $-90^\circ$  direction in the RS and the  $-90^\circ$  direction in the TS coincide spatially. Moreover, we assume that the use of tunnel-diode-based circuitry enables sufficiently fast reconfiguration of metasurface parameters, such that user angles can be treated as quasi-static over the data acquisition interval. The considered geometry is illustrated in Fig. 1, where angles outside

<sup>1</sup>Boldface letters represent vectors or matrices.  $\mathbb{C}$  and  $\mathbb{R}$  are the sets of complex numbers and real numbers, respectively.  $|\cdot|$  represents either the modulus of a complex number or cardinality of a set. The symbols  $\mathbf{x}^T$ ,  $\mathbf{x}^*$ ,  $\mathbf{x}^H$  represent the transpose, complex conjugate, and Hermitian of  $\mathbf{x}$ .  $\mathbf{0}_n$  denotes the null vector,  $\mathbf{O}_{n \times m}$  the null matrix, and  $\mathbf{I}_n$  the identity matrix.  $\mathbf{1}_n$  denotes the  $n$ -dimensional all-ones column vector. The element of matrix  $\mathbf{A}$  positioned at the intersection of the  $i$ -th row and the  $\ell$ -th column is denoted by  $\{\mathbf{A}\}_{i,\ell}$ .  $\text{Diag}[\mathbf{A}]$  represents the vector formed by the diagonal entries of the matrix  $\mathbf{A}$ , whereas  $\text{diag}[\mathbf{a}]$  represents the diagonal matrix constructed from the elements of the vector  $\mathbf{a}$ . The operation  $\mathbf{B} = \text{blkdiag}[\mathbf{A}_1, \dots, \mathbf{A}_n]$  returns the block diagonal matrix created by aligning the input matrices  $\mathbf{A}_1, \dots, \mathbf{A}_N$  along the diagonal of  $\mathbf{B}$ . The vectorization of a matrix  $\mathbf{A} \in \mathbb{C}^{n \times m}$ , denoted  $\text{vec}(\mathbf{A})$ , is the  $(nm)$ -dimensional column vector obtained by stacking the columns of  $\mathbf{A}$  on top of one another. The rank of a matrix  $\mathbf{A}$  is denoted by  $\text{rank}[\mathbf{A}]$ ;  $\text{ker}(\mathbf{A})$  denotes the kernel (null space) of the matrix  $\mathbf{A}$ .  $\|\cdot\|_2$  and  $\|\cdot\|_F$  represent the vector  $l_2$  norm and matrix Frobenius norm. The  $i$ -th singular values of matrix  $\mathbf{A}$  is indicated as  $\sigma_i^2(\mathbf{A})$ .  $\lfloor \cdot \rfloor$  and  $\lceil \cdot \rceil$  represent the floor and ceiling functions, respectively.  $\arg(\cdot)$  represents the phase angle of a complex number. The symbols  $\otimes$  and  $\odot$  represent Kronecker and Hadamard product, respectively. If  $\mathbf{D}_1$  and  $\mathbf{D}_2$  are non-singular diagonal conformable matrices, the matrix  $\mathbf{D}_1 \otimes \mathbf{D}_2$  results in another diagonal matrix where each diagonal element is the quotient of the corresponding elements from  $\mathbf{D}_1$  and  $\mathbf{D}_2$ .

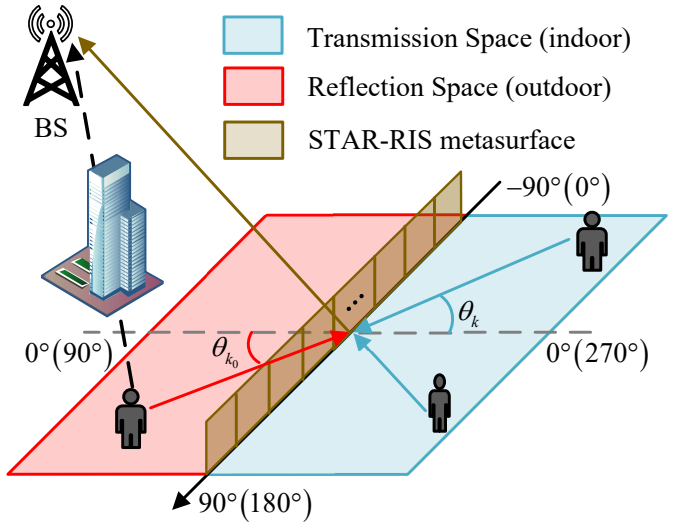


Fig. 1. Schematic diagram of the STAR-RIS-assisted system.

the brackets follow the semi-space notation, whereas angles inside the brackets correspond to the full-space notation.

#### A. STAR-RIS model

The STAR-RIS coefficients can be updated on a slot-by-slot basis, thus yielding a slot-dependent effective sensing matrix. Such a temporal reconfiguration increases measurement diversity and improves identifiability of the angle parameters, particularly with a single RF sensing chain. It can also facilitate separation of the coupled reflection/transmission components for full-space DOA recovery. We assume the reconfiguration is sufficiently fast so that user angles are quasi-static over  $T_s$  slots, while the STAR-RIS control sequence is known.

In this work, the considered STAR-RIS adopts an ES working mode, i.e., the electromagnetic response of the  $n$ -th element during the  $t$ -th slot can be described by the transmission coefficient and reflection coefficient as

$$\phi_{i,n}(t) = \beta_{i,n}(t) e^{j\varphi_{i,n}(t)}, \text{ for } i \in \{T, R\} \quad (1)$$

where  $0 < \beta_{i,n}(t) \leq 1$  and  $\varphi_{i,n}(t) \in [0, 2\pi)$  represent the amplitude and phase of the  $n$ -th RIS element, respectively, for  $n \in \mathcal{N} \triangleq \{1, 2, \dots, N\}$  and  $t \in \mathcal{T} \triangleq \{1, 2, \dots, T_s\}$ .

In the ES mode, the passive lossless STAR-RIS must satisfy two constraints. First, the principle of power conservation dictates that the incident signal power on each element must equal the sum of the reflected and transmitted power. Second, the  $n$ -th STAR-RIS element's purely reactive impedance (both electric and magnetic) governs the phase relationship between its reflection and transmission coefficients which must obey  $\cos(\varphi_{R,n}(t) - \varphi_{T,n}(t)) = 0$ . Hence, the constraints are

$$\beta_{R,n}^2(t) + \beta_{T,n}^2(t) = 1 \quad (2)$$

$$\Delta\varphi_n(t) \triangleq \varphi_{R,n}(t) - \varphi_{T,n}(t) = \frac{\pi}{2} \text{ or } \frac{3\pi}{2}. \quad (3)$$

In what follows, the STAR-RIS is collectively described by the matrices  $\Phi_R(t) \in \mathbb{C}^{N \times N}$  and  $\Phi_T(t) \in \mathbb{C}^{N \times N}$ , gathering

the reflection and transmission coefficients of the STAR-RIS, respectively, which are given by

$$\Phi_i(t) \triangleq \text{diag} \left[ \beta_{i,1}(t) e^{j\varphi_{i,1}(t)}, \dots, \beta_{i,N}(t) e^{j\varphi_{i,N}(t)} \right] \quad (4)$$

for  $i \in \{\text{T}, \text{R}\}$  and  $t \in \mathcal{T}$ .

The phase-difference constraint (3) constitutes a binary decision problem, formally expressed as  $e^{j\varphi_{p,n}(t)} = \pm j e^{j\varphi_{q,n}(t)}$ , for  $p, q \in \{\text{T}, \text{R}\}$  and  $p \neq q$ . The amplitude information is subject to constraint (2), satisfying  $\beta_{p,n}(t) = [1 - \beta_{q,n}^2(t)]^{1/2}$ . Therefore, at the  $n$ -th element of the metasurface, the complex scattering parameters obey

$$\beta_{p,n}(t) e^{j\varphi_{p,n}(t)} = \pm j \sqrt{1 - \beta_{q,n}^2(t)} e^{j\varphi_{q,n}(t)} \quad (5)$$

for each  $n \in \mathcal{N}$ ,  $t \in \mathcal{T}$ ,  $p, q \in \{\text{T}, \text{R}\}$  and  $p \neq q$ . Extending the element-wise formulation to matrix form yields the generalized mapping rule

$$\Phi_p(t) = [\mathbf{I}_N - \mathbf{B}_q^2(t)]^{1/2} \oslash \mathbf{B}_q(t) \odot \mathbf{J}(t) \odot \Phi_q(t), \quad \text{for } p, q \in \{\text{T}, \text{R}\} \text{ and } p \neq q \quad (6)$$

where  $\mathbf{J}(t) \triangleq \text{diag}[j_1(t), j_2(t), \dots, j_N(t)]$ , with  $j_n(t) = \pm j$ , and  $\mathbf{B}_q(t) \triangleq \text{diag}[\beta_{q,1}(t), \beta_{q,2}(t), \dots, \beta_{q,N}(t)]$ .

### B. Signal model at the base station

Let us assume that all users located in the far-field region of the STAR-RIS, with their azimuth angles relative to the metasurface array denoted as  $\theta_1, \theta_2, \dots, \theta_K$ . The steering vector of the  $k$ -th user can be expressed as

$$\mathbf{a}(\theta_k) \triangleq \left[ 1, e^{-j\pi \sin \theta_k}, \dots, e^{-j\pi(N-1) \sin \theta_k} \right]^T. \quad (7)$$

Under the narrowband assumption, the contribution of the  $k$ -th user is represented by the spatial signature  $\mathbf{a}(\theta_k)$  multiplied by a scalar coefficient  $s_k(t)$ . During the sensing stage, we consider pilot-aided signaling (or a short acquisition window) so that  $s_k(t)$  can be treated as a slot-invariant complex gain  $s_k$  [32], [33], without affecting DOA recovery. Therefore, let  $\mathcal{K}_{\text{R}} \triangleq \{1, 2, \dots, K_{\text{R}}\}$  and  $\mathcal{K}_{\text{T}} \triangleq \{K_{\text{R}} + 1, K_{\text{R}} + 2, \dots, K\}$ , the impinging signal at the STAR-RIS in each slot reads as

$$\mathbf{x}_i = \sum_{k \in \mathcal{K}_i} \mathbf{a}(\theta_k) s_k = \mathbf{A}_i \mathbf{s}_i, \quad \text{for } i \in \{\text{T}, \text{R}\} \quad (8)$$

for  $t \in \mathcal{T}$ , with

$$\mathbf{A}_{\text{R}} \triangleq [\mathbf{a}(\theta_1), \dots, \mathbf{a}(\theta_{K_{\text{R}}})] \in \mathbb{C}^{N \times K_{\text{R}}} \quad (9)$$

$$\mathbf{A}_{\text{T}} \triangleq [\mathbf{a}(\theta_{K_{\text{R}}+1}), \dots, \mathbf{a}(\theta_K)] \in \mathbb{C}^{N \times K_{\text{T}}} \quad (10)$$

$$\mathbf{s}_{\text{R}} \triangleq [s_1, \dots, s_{K_{\text{R}}}]^T \in \mathbb{C}^{K_{\text{R}}} \quad (11)$$

$$\mathbf{s}_{\text{T}} \triangleq [s_{K_{\text{R}}+1}, \dots, s_K]^T \in \mathbb{C}^{K_{\text{T}}}. \quad (12)$$

Consequently, the data collected by the BS is given by

$$y(t) = \mathbf{h}^T [\Phi_{\text{R}}(t) \mathbf{x}_{\text{R}} + \Phi_{\text{T}}(t) \mathbf{x}_{\text{T}}] + n(t) \quad (13)$$

where  $\mathbf{h} \triangleq [h_1, \dots, h_N]^T \in \mathbb{C}^N$  represents the channel between the STAR-RIS and the BS, which is assumed to be time-invariant over  $T_s$  consecutive slots and known at the BS, whereas  $n(t) \sim \mathcal{CN}(0, \sigma_n^2)$  is additive white Gaussian noise.

Exploiting the bijective mapping (6), the BS data can be expressed using a single operator, e.g.,  $\Phi_{\text{R}}(t)$ , thus yielding

$$y(t) = \mathbf{h}^T \Phi_{\text{R}}(t) \sum_{k=1}^K \tilde{\mathbf{a}}(t; \theta_k) s_k + n(t) = \mathbf{h}^T \Phi_{\text{R}}(t) \tilde{\mathbf{A}}(t) \mathbf{s} + n(t) \quad (14)$$

with  $\tilde{\mathbf{a}}(t; \theta_k) \triangleq \mathbf{j}_k(t) \odot \mathbf{p}_k(t) \odot \mathbf{a}(\theta_k) \in \mathbb{C}^N$ , where  $\mathbf{j}_k(t)$  and  $\mathbf{p}_k(t)$  are the phase and amplitude correction vectors, respectively, which are defined as

$$\mathbf{j}_k(t) \triangleq \begin{cases} \mathbf{1}_N^T, & \text{for } k \in \mathcal{K}_{\text{R}}; \\ [j_1(t), \dots, j_N(t)]^T, & \text{for } k \in \mathcal{K}_{\text{T}}; \end{cases} \quad (15)$$

$$\mathbf{p}_k(t) \triangleq \begin{cases} \mathbf{1}_N^T, & \text{for } k \in \mathcal{K}_{\text{R}}; \\ [p_1(t), \dots, p_N(t)]^T, & \text{for } k \in \mathcal{K}_{\text{T}}; \end{cases} \quad (16)$$

with  $p_n(t) \triangleq [1 - \beta_{R,n}^2(t)]^{1/2} / \beta_{R,n}(t)$ , and, finally, we have defined the matrix  $\tilde{\mathbf{A}}(t) \triangleq [\tilde{\mathbf{a}}(t; \theta_1), \dots, \tilde{\mathbf{a}}(t; \theta_K)] \in \mathbb{C}^{N \times K}$ , for  $t \in \mathcal{T}$ , and the vector  $\mathbf{s} \triangleq [\mathbf{s}_{\text{R}}^T, \mathbf{s}_{\text{T}}^T]^T \in \mathbb{C}^K$ .

### III. FULL-SPACE DOA ESTIMATION UNDER ELEMENT-WISE UNIFORM STAR-RIS PARAMETERS

Herein, we first consider the *element-wise uniform* STAR-RIS regime, where all metasurface elements employ identical parameters, i.e.,  $\beta_{i,1}(t) = \beta_{i,2}(t) = \dots = \beta_{i,N}(t)$  and  $\Delta\varphi_1(t) = \Delta\varphi_2(t) = \dots = \Delta\varphi_N(t)$ . Equivalently,  $\beta_{i,n}(t) = \beta_i(t)$  and  $\Delta\varphi_n(t) = \Delta\varphi(t)$ ,  $\forall n \in \mathcal{N}$  and  $t \in \mathcal{T}$ . In this case, by virtue of (15) and (16), we may partition

$$\tilde{\mathbf{A}}(t) = [\mathbf{A}_{\text{R}}, g(t) \mathbf{A}_{\text{T}}] \quad (17)$$

with  $g(t) \triangleq \pm j [1 - \beta_{\text{R}}^2(t)]^{1/2} / \beta_{\text{R}}(t)$ . Substituting (17) in (14), we get the equivalent signal model

$$y(t) = \mathbf{h}^T \Phi_{\text{R}}(t) \mathbf{r}(t) + n(t) \quad (18)$$

where  $\mathbf{r}(t) \triangleq \mathbf{A} \tilde{\mathbf{s}}(t) \in \mathbb{C}^N$ , with  $\mathbf{A} \triangleq [\mathbf{A}_{\text{R}}, \mathbf{A}_{\text{T}}] \in \mathbb{C}^{N \times K}$  and  $\tilde{\mathbf{s}}(t) \triangleq [\mathbf{s}_{\text{R}}^T, g(t) \mathbf{s}_{\text{T}}^T]^T \in \mathbb{C}^K$ , for  $t \in \mathcal{T}$ .

#### A. Annihilation of the vector $\mathbf{r}(t)$

In this study, we adopt a FRI perspective [37]–[40] to model the STAR-RIS-aided sensing data. The key observation is that the data received by the BS in (18) can be regarded as linear measurements of a line-spectrum sequence defined over the metasurface aperture. Indeed, the contribution of the  $k$ -th user to the  $n$ -th entry  $r_n(t)$  of the vector  $\mathbf{r}(t)$  is given by  $\tilde{s}_k(t) z_k^{n-1}$ , for  $n \in \mathcal{N}$  and  $t \in \mathcal{T}$ , with  $z_k \triangleq e^{-j\pi \sin \theta_k}$ . Accordingly, the superposition of  $K$  users across the  $N$  metasurface sampling points admits the line-spectrum form

$$r_n(t) = \sum_{k=1}^K \tilde{s}_k(t) z_k^{n-1}, \quad \text{for } n \in \mathcal{N} \quad (19)$$

where the unknown DOAs are embedded in  $z_1, z_2, \dots, z_K$ . Therefore, the DOA estimation problem is converted into a line-spectrum recovery task with only  $K$  degrees of freedom (the source angles and gains), while the observations are uniformly indexed over the metasurface aperture. Such a structured representation enables gridless recovery via algebraic tools (e.g., annihilating filters and polynomial rooting).

Let us construct a  $K$ -th order annihilating polynomial

$$C(z) = \prod_{k=1}^K (1 - z_k^{-1}z) = \sum_{m=0}^K c_m z^m \quad (20)$$

whose roots are given by  $z_1, z_2, \dots, z_K$ , i.e.,  $C(z_k) = 0$ . Then, we observe that, for any shift  $\nu$  such that the indices remain within the set  $\mathcal{N}$ , the sequence  $r_n(t)$  obeys

$$\sum_{m=0}^K c_m r_{m+\nu}(t) = 0, \quad \text{for } \nu \in \{1, 2, \dots, N-K\}. \quad (21)$$

Indeed, for each  $t \in \mathcal{T}$ , one has

$$\begin{aligned} \sum_{m=0}^K c_m r_{m+\nu}(t) &= \sum_{m=0}^K c_m \sum_{k=1}^K \tilde{s}_k(t) e^{-j\pi(m+\nu-1)\sin\theta_k} \\ &= \sum_{k=1}^K \tilde{s}_k(t) e^{-j\pi(\nu-1)\sin\theta_k} \sum_{m=0}^K c_m e^{-j\pi m \sin\theta_k} \\ &= \sum_{k=1}^K \tilde{s}_k(t) e^{-j\pi(\nu-1)\sin\theta_k} C(z_k) = 0 \end{aligned} \quad (22)$$

where the last equality follows from  $C(z_k) = 0$ . Such equations can be compactly written in matrix form as follows

$$\mathbf{H}_K(\mathbf{r}(t)) \mathbf{c} = \mathbf{0}_{N-K}, \quad \text{for } t \in \mathcal{T} \quad (23)$$

with

$$\mathbf{H}_K(\mathbf{r}(t)) \triangleq \begin{bmatrix} r_1(t) & r_2(t) & \cdots & r_{K+1}(t) \\ r_2(t) & r_3(t) & \cdots & r_{K+2}(t) \\ \vdots & \vdots & \ddots & \vdots \\ r_{N-K}(t) & r_{N-K+1}(t) & \cdots & r_N(t) \end{bmatrix} \quad (24)$$

representing the reordering matrix characterized by a Hankel structure and  $\mathbf{c} \triangleq [c_0, \dots, c_K]^T \in \mathbb{C}^{K+1}$ . The linear system in (23) corresponds to the *annihilating-filter (AF)* equation, which holds for each time slot  $t \in \mathcal{T}$ .

Let  $\mathbf{R} \triangleq [\mathbf{r}(1), \dots, \mathbf{r}(T_s)] \in \mathbb{C}^{N \times T_s}$  and  $\mathbf{r} \triangleq \text{vec}(\mathbf{R})$ , the multi-slot counterpart of (23) is given by

$$\underbrace{\begin{bmatrix} \mathbf{H}_K(\mathbf{r}(1)) \\ \vdots \\ \mathbf{H}_K(\mathbf{r}(T_s)) \end{bmatrix}}_{\mathbf{H}_K^{\text{stack}}(\mathbf{r})} \mathbf{c} = \mathbf{0}_{(N-K)T_s}. \quad (25)$$

Since  $\mathbf{H}_K^{\text{stack}}(\mathbf{r}) \in \mathbb{C}^{(N-K)T_s \times (K+1)}$  is of rank  $K$ , the vector  $\mathbf{c}$  lies in its nullspace. Thus, we can obtain  $\mathbf{c}$  by performing a singular value decomposition (SVD) on  $\mathbf{H}_K^{\text{stack}}(\mathbf{r})$  and choosing the right singular vector corresponding to its zero (smallest) singular value. Substituting  $\mathbf{c}$  into (20) determines  $C(z)$ , and the user angles can then be recovered from its roots.

### B. Proximal gradient descent method

For each slot  $t \in \mathcal{T}$ , the latent vector  $\mathbf{r}(t)$  admits a FRI structure and, thus, satisfies the AF relations in (23)–(38). However, the vector  $\mathbf{r}(t)$  is *not* directly observed at the BS. Instead, the BS collects only its slot-dependent linear projection in (18). Consequently, estimating the annihilating

filter  $\mathbf{c}$  (and hence the DOAs) requires first recovering an accurate, denoised version of the underlying FRI vector  $\mathbf{r}$  from the measurements  $\mathbf{y} \triangleq [y(1), \dots, y(T_s)]^T \in \mathbb{C}^{T_s}$ . To resolve this problem, we design a proximal gradient descent (PGD)-based framework [44], [45] capable of robustly estimating the underlying parameters in  $\mathbf{r}$  from the observed data block  $\mathbf{y}$ .

By virtue of (18), one has

$$\mathbf{y} = \Phi \mathbf{r} + \mathbf{n} \quad (26)$$

where  $\Phi \triangleq \text{blkdiag}[\mathbf{h}^T \Phi_R(1), \dots, \mathbf{h}^T \Phi_R(T_s)] \in \mathbb{C}^{T_s \times NT_s}$  and  $\mathbf{n} \triangleq [n(1), \dots, n(T_s)]^T \in \mathbb{C}^{T_s}$ . We introduce an auxiliary vector  $\mathbf{b} \triangleq [\mathbf{b}^T(1), \dots, \mathbf{b}^T(T_s)]^T \in \mathbb{C}^{NT_s}$ , which is meant to represent the latent vector  $\mathbf{r}$ . In our optimization framework, the vector  $\mathbf{b}$  plays the role of the unknown  $\mathbf{r}$ , provided that the FRI structure is enforced on  $\mathbf{b}$ . To this aim, we introduce the matrix  $\mathbf{H}_\alpha^{\text{stack}}(\mathbf{b}) \in \mathbb{C}^{(N-\alpha)T_s \times (\alpha+1)}$ , which is obtained similarly to  $\mathbf{H}_K^{\text{stack}}(\mathbf{r})$  in (25) by substituting  $K$  with  $\alpha$ , and replacing  $\mathbf{r}(1), \mathbf{r}(2), \dots, \mathbf{r}(T_s)$  with  $\mathbf{b}(1), \mathbf{b}(2), \dots, \mathbf{b}(T_s)$ , respectively, with  $\mathbf{H}_\alpha(\mathbf{b}(t))$  obtained from (24) by using  $\alpha$  and  $\mathbf{b}(t)$  in lieu of  $K$  and  $\mathbf{r}(t)$ , respectively. Regarding the choice of  $\alpha$ , we need  $\mathbf{H}_\alpha^{\text{stack}}(\mathbf{b})$  to be “tall enough” and “wide enough” to reveal rank  $K$ . A common practical requirement is  $\alpha \geq K$  and  $N - \alpha > 0$ , which leads to the inequality  $K \leq \alpha < N$ .

The latent vector  $\mathbf{r}$  can be estimated from  $\mathbf{y}$  by solving the constrained optimization problem

$$\begin{aligned} \hat{\mathbf{r}} &= \arg \min_{\mathbf{b} \in \mathbb{C}^{NT_s}} \|\mathbf{y} - \Phi \mathbf{b}\|_2^2, \quad \text{subject to (s.t.)} \\ \text{rank}(\mathbf{H}_\alpha^{\text{stack}}(\mathbf{b})) &\leq K \end{aligned} \quad (27)$$

where the constraint forces  $\mathbf{b}$  to be consistent with a  $K$ -source FRI model that inherently guarantees the existence of a nontrivial null space, from which the vector  $\mathbf{c}$  can be computed. Problem (27) is transformed into an equivalent unconstrained optimization formulation

$$\hat{\mathbf{r}} = \arg \min_{\mathbf{b} \in \mathbb{C}^{NT_s}} \{\|\mathbf{y} - \Phi \mathbf{b}\|_2^2 + \delta_{\mathbb{H}_K} [\mathbf{H}_\alpha^{\text{stack}}(\mathbf{b})]\} \quad (28)$$

by introducing the indicator function for a matrix  $\mathbf{A}$

$$\delta_{\mathbb{H}_K} [\mathbf{A}] \triangleq \begin{cases} 0, & \text{rank}[\mathbf{A}] \leq K; \\ +\infty, & \text{otherwise.} \end{cases} \quad (29)$$

We adopt a PGD-based scheme [44], [45] to solve problem (28). Given  $\mathbf{b}^{(i)}$  at iteration  $i$ , a gradient step on the smooth term  $\|\mathbf{y} - \Phi \mathbf{b}\|_2^2$  yields the iterative rule

$$\Delta \mathbf{b}^{(i)} = \mathbf{b}^{(i)} + 2\mu_1 \Phi^H (\mathbf{y} - \Phi \mathbf{b}^{(i)}) \quad (30)$$

where  $\mu_1 > 0$  is the step-size. The next iterate is obtained through the proximal map associated with the Hankel-rank constraint. So doing, the update rule for vector  $\mathbf{b}$  is given by  $\mathbf{b}^{(i+1)} = \text{prox}_\mu(\Delta \mathbf{b}^{(i)})$ , with

$$\begin{aligned} \text{prox}_\mu(\Delta \mathbf{b}^{(i)}) &\triangleq \arg \min_{\mathbf{z} \in \mathbb{C}^{NT_s}} \left\{ \frac{1}{2\mu_1} \|\Delta \mathbf{b}^{(i)} - \mathbf{z}\|_2^2 \right. \\ &\quad \left. + \delta_{\mathbb{H}_K} (\mathbf{H}_\alpha^{\text{stack}}(\mathbf{z})) \right\}. \end{aligned} \quad (31)$$

Because the rank constraint is nonconvex, we approximate (31) via *alternating projections* in the matrix space [46], i.e.,

$$\text{prox}_\mu(\Delta \mathbf{b}^{(i)}) \approx \Pi_{\mathcal{H}_\alpha^{\text{stack}}}^{-1} \left( \Pi_{\mathcal{H}_\alpha^{\text{stack}}} \left( \Pi_{\mathcal{R}_K} \left( \mathbf{H}_\alpha^{\text{stack}}(\Delta \mathbf{b}^{(i)}) \right) \right) \right) \quad (32)$$

where the vector  $\Delta\mathbf{b}^{(i)}$  is first mapped to the block-Hankel matrix  $\mathbf{H}_\alpha^{\text{stack}}(\Delta\mathbf{b}^{(i)})$ ,  $\Pi_{\mathcal{R}_K}(\cdot)$  denotes the rank- $K$  projection, and  $\Pi_{\mathcal{H}_\alpha^{\text{stack}}}^{-1}(\cdot)$  is the inverse Hankel operator that maps the block-Hankel matrix back to a vector of  $\mathbb{C}^{NT_s}$ . Concretely, for a matrix  $\mathbf{Q}_\alpha^{\text{stack}} \in \mathbb{C}^{(N-\alpha)T_s \times (\alpha+1)}$ , whose SVD is given by  $\mathbf{Q}_\alpha^{\text{stack}} = \mathbf{U}\Lambda\mathbf{V}^H$ , the rank- $K$  projection is defined as

$$\mathbf{Q}_K^{\text{stack}} = \Pi_{\mathcal{R}_K}(\mathbf{Q}_\alpha^{\text{stack}}) = \mathbf{U}\Lambda_K\mathbf{V}^H \quad (33)$$

where  $\Lambda_K$  retains only the  $K$  largest singular values. It is noteworthy that (33) represents best rank- $K$  approximation of  $\mathbf{Q}_\alpha^{\text{stack}}$  in Frobenius norm [47]. The rank- $K$  SVD truncation of  $\mathbf{H}_\alpha^{\text{stack}}(\Delta\mathbf{b}^{(i)})$  is not exactly stacked Hankel in general, yet it is guaranteed to be close to the stacked-Hankel set when  $\mathbf{H}_\alpha^{\text{stack}}(\Delta\mathbf{b}^{(i)})$  is a small perturbation of a low-rank stacked-Hankel matrix (see Appendix A for the formal proof). The projection  $\Pi_{\mathcal{H}_\alpha^{\text{stack}}}(\cdot)$  is implemented block-wise to restore block-Hankel structure. Let  $\mathbf{Q}_K^{\text{stack}} = [\mathbf{Q}_{K,1}^T, \dots, \mathbf{Q}_{K,T_s}^T]^T$ , we perform anti-diagonal averaging (also called ‘‘Hankelization’’) of each sub-block separately, i.e.,

$$\Pi_{\mathcal{H}_\alpha^{\text{stack}}}(\mathbf{Q}_K^{\text{stack}}) = [\Pi_{\mathcal{H}_\alpha}(\mathbf{Q}_{K,1})^T, \dots, \Pi_{\mathcal{H}_\alpha}(\mathbf{Q}_{K,T_s})^T]^T \quad (34)$$

where  $\Pi_{\mathcal{H}_\alpha}(\cdot)$  replaces all entries on the same anti-diagonal by their average. Such alternating projections ensure that the resulting vector not only satisfies both convex and non-convex indicator constraints but also lies within a predefined Euclidean distance tolerance.

The alternating-projection loop is terminated when either  $\|\mathbf{b}^{(i+1)} - \mathbf{b}^{(i)}\|_2 \leq \varepsilon$ , for a tolerance  $\varepsilon > 0$ , or a maximum number of iterations  $I_{\max}$  is reached. After convergence, the estimate  $\hat{\mathbf{r}}$  of the latent vector  $\mathbf{r}$  is provided. Subsequently, an estimate of the annihilating filter  $\mathbf{c}$  is obtained from the null space of  $\mathbf{H}_\alpha^{\text{stack}}(\hat{\mathbf{r}})$ , e.g., as the right singular vector associated with the smallest singular value. The polynomial  $\hat{C}(z)$  is then formed using these coefficients, and the DOAs are recovered via polynomial root finding. The annihilating polynomial  $\hat{C}(z)$  generally has more than  $K$  roots. In practice, only the  $K$  roots corresponding to physical sources are retained, which are identified as those lying closest to the unit circle (or, equivalently, having magnitude closest to one); the remaining roots are spurious and are discarded. The overall flow of the proposed method is outlined by Algorithm 1.

#### IV. FULL-SPACE DOA ESTIMATION UNDER NONUNIFORM ENERGY-SPLITTING STAR-RIS PARAMETERS

Although the STAR-RIS parameters are programmable, enforcing identical settings across all elements can be overly restrictive. In practice, improving communication throughput and sensing accuracy often calls for additional degrees of freedom in the metasurface design, particularly in the allocation of reflection/transmission power. Under narrowband operation with identical unit cells, the reflection-transmission phase offset is primarily determined by the element design and is approximately invariant across the array [48]. Henceforth, we consider herein a more general regime in which the phase difference is common across the metasurface, while the ES coefficients are allowed to vary across elements.

---

**Algorithm 1:** FRI-based DOA estimation for element-wise uniform STAR-RIS

---

```

INPUT:  $\mathbf{y}, N, T_s, K, \alpha, \mu_1, I_{\max}, \varepsilon$ 
OUTPUT:  $\hat{\theta}_1, \dots, \hat{\theta}_K$ 
Initialize  $\mathbf{b}^{(0)}$ 
for  $i = 1, 2, \dots, I_{\max}$  do
     $\Delta\mathbf{b}^{(i)} \leftarrow \mathbf{b}^{(i)} + 2\mu_1 \Phi^H(\mathbf{y} - \Phi\mathbf{b}^{(i)})$ 
     $\mathbf{b}^{(i+1)} \leftarrow \Pi_{\mathcal{H}_\alpha^{\text{stack}}}^{-1}(\Pi_{\mathcal{H}_\alpha^{\text{stack}}}(\Pi_{\mathcal{R}_K}(\mathbf{H}_\alpha^{\text{stack}}(\Delta\mathbf{b}^{(i)}))))$ 
    if  $\|\mathbf{b}^{(i)} - \mathbf{b}^{(i+1)}\| \leq \varepsilon$  then  $\hat{\mathbf{r}} = \mathbf{b}^{(i+1)}$  break
    else
         $\hat{\mathbf{r}} = \mathbf{b}^{(i+1)}$ 
         $i = i + 1$ 
    end for
     $\mathbf{U}, \mathbf{S}, \mathbf{V} \leftarrow \text{SVD}(\mathbf{H}_\alpha^{\text{stack}}(\hat{\mathbf{r}}))$ 
     $\hat{C}(z) \leftarrow \hat{\mathbf{c}} = \mathbf{V}(:, \alpha + 1)$ 
    Keep the  $K$  roots  $\{\hat{z}_k\}_{k=1}^K$  of  $\hat{C}(z)$  closest to unit circle
     $\hat{\theta}_k = -\arcsin(\arg(\hat{z}_k)/\pi)$  for  $k \in \{1, 2, \dots, K\}$ 

```

---

By virtue of (15) and (16), we may partition

$$\tilde{\mathbf{A}}(t) = [\mathbf{A}_R, \mathbf{G}(t) \mathbf{A}_T] \quad (35)$$

with  $\mathbf{G}(t) \triangleq \pm j \text{diag}[p_1(t), \dots, p_N(t)]$ . Substituting (35) in (14), we get the equivalent signal model

$$y(t) = \psi^T(t) \mathbf{x} + n(t) \quad (36)$$

where  $\psi(t) \triangleq [\mathbf{I}_N, \mathbf{G}(t)]^T \Phi_R(t) \mathbf{h} \in \mathbb{C}^{2N}$  and, remembering (8), we have defined the vector  $\mathbf{x} \triangleq [\mathbf{x}_R^T, \mathbf{x}_T^T]^T \in \mathbb{C}^{2N}$ . Collecting all the measurements in the vector  $\mathbf{y}$ , one gets

$$\mathbf{y} = \Psi^T \mathbf{x} + \mathbf{n} \quad (37)$$

with  $\Psi \triangleq [\psi(1), \dots, \psi(T_s)] \in \mathbb{C}^{(2N) \times T_s}$ , where  $\mathbf{n}$  has been already defined in Subsection III-B together with  $\mathbf{y}$ .

##### A. Annihilation of the vector $\mathbf{x}$

Although the element-wise ES coefficients vary, the reflected and transmitted components still admit *parallel* FRI-type representations. Specifically, along the same lines of Subsection III-A, it can be verified that the following AF matrix equation holds

$$\mathbf{H}_{K_i}(\mathbf{x}_i) \mathbf{c}_i = \mathbf{0}_{N-K_i} \text{ for } i \in \{T, R\} \quad (38)$$

where the Hankel matrix  $\mathbf{H}_{K_i}(\mathbf{x}_i) \in \mathbb{C}^{(N-K_i) \times (K_i+1)}$  is obtained from (24) by replacing  $K$  and  $\mathbf{r}(t)$  with  $K_i$  and  $\mathbf{x}_i$ , respectively, and  $\mathbf{c}_i \in \mathbb{C}^{K_i+1}$  gathers the annihilation coefficients. Since each entry of  $\mathbf{x}_i$  is a superposition of a finite number of complex exponentials, the corresponding Hankel matrix is low rank, i.e.,  $\text{rank}(\mathbf{H}_{K_i}(\mathbf{x}_i)) = K_i$ , for  $i \in \{T, R\}$ . Hence, the vector  $\mathbf{c}_i$  can be recovered as the right singular vector corresponding to the zero (smallest) singular value of  $\mathbf{H}_{K_i}(\mathbf{x}_i)$ . The user angles can then be recovered from the roots of the polynomial  $C_i(z)$  whose coefficients are the entries of  $\mathbf{c}_i$ . In the proposed algorithm, the two AF constraints in (38) are not imposed independently. Instead, as described in Subsection IV-B, they are enforced jointly by means of a single horizontally concatenated lifting operator.

### B. Proximal gradient descent method

DOA recovery cannot proceed directly from  $\mathbf{y}$ . Indeed, we must first infer a denoised estimate of the latent FRI vector  $\mathbf{x}$  from the observations in  $\mathbf{y}$ , after which the annihilating filters  $\mathbf{c}_R$  and  $\mathbf{c}_T$  are obtained and the angles are extracted. To this end, we introduce the auxiliary vector  $\boldsymbol{\beta} \triangleq [\boldsymbol{\beta}_R^T, \boldsymbol{\beta}_T^T]^T \in \mathbb{C}^{2N}$ , which plays the role of a denoised estimate of  $\mathbf{x}$ . With this goal in mind, let us introduce the matrix  $\mathbf{H}_\alpha(\boldsymbol{\beta}_i) \in \mathbb{C}^{(N-\alpha) \times (\alpha+1)}$ , with  $K \leq \alpha < N$ , from (24) obtained by replacing  $K$  and  $\mathbf{r}(t)$  with  $\alpha$  and  $\boldsymbol{\beta}_i$ , respectively, for  $i \in \{R, T\}$ . We then define the *horizontally stacked* lifting

$$\mathbf{H}_\alpha^{\text{pair}}(\boldsymbol{\beta}) \triangleq [\mathbf{H}_\alpha(\boldsymbol{\beta}_R) \ \mathbf{H}_\alpha(\boldsymbol{\beta}_T)] \in \mathbb{C}^{(N-\alpha) \times 2(\alpha+1)}. \quad (39)$$

Under the FRI generative model, the matrix  $\mathbf{H}_\alpha^{\text{pair}}(\boldsymbol{\beta})$  has rank at most  $K = K_R + K_T$ .

Reasoning as in Subsection III-B, one ends up to solve the unconstrained optimization formulation

$$\hat{\mathbf{x}} = \arg \min_{\boldsymbol{\beta} \in \mathbb{C}^{2N}} \{ \|\mathbf{y} - \boldsymbol{\Psi}^T \boldsymbol{\beta}\|_2^2 + \delta_{\mathbb{H}_K} [\mathbf{H}_\alpha^{\text{pair}}(\boldsymbol{\beta})] \} \quad (40)$$

where the indicator function  $\delta_{\mathbb{H}_K}(\cdot)$  is defined in (29) and enforces the rank- $K$  FRI prior on the horizontally stacked lifting. The PGD solver for (40) follows the same derivation steps as in Subsection III-B and is therefore omitted for brevity. In particular, we perform a gradient step on the quadratic data-fidelity term  $\|\mathbf{y} - \boldsymbol{\Psi}^T \boldsymbol{\beta}\|_2^2$ , and approximate the resulting proximal update associated with the structured low-rank constraint through alternating projections in the lifted domain. Unlike the element-wise uniform regime, the operator  $\Pi_{\mathcal{H}_\alpha^{\text{pair}}}^{-1}(\cdot)$  maps the horizontally stacked lifting matrix back to two vectors of  $\mathbb{C}^N$ , whereas  $\Pi_{\mathcal{R}_K}(\cdot)$  performs rank- $K$  projection as in (33). We note that the rank- $K$  truncation obtained by SVD on  $\mathbf{H}_\alpha^{\text{pair}}(\Delta \boldsymbol{\beta}^{(i)})$  does not, in general, preserve the horizontal-stacked Hankel structure exactly. Nevertheless, when  $\mathbf{H}_\alpha^{\text{pair}}(\Delta \boldsymbol{\beta}^{(i)})$  can be expressed as a small perturbation of an ideal low-rank horizontal-stacked Hankel matrix, its rank- $K$  SVD approximation is guaranteed to lie in a neighborhood of the horizontal-stacked Hankel set (in Frobenius norm). This fact follows from standard best low-rank approximation and perturbation arguments (e.g., Eckart-Young-Mirsky and singular-value perturbation bounds), and the proof proceeds similarly to Appendix A. The overall implementation steps of the proposed estimation procedure are provided in Algorithm 2, where  $\mu_2 > 0$  is the step-size of the PGD algorithm.

## V. PARAMETER SETTING AND PERFORMANCE ANALYSIS

The performance of the proposed algorithm depends critically on two design parameters: the PGD step-size and the Hankel parameter that sets the lifting dimension. These choices jointly govern the convergence behavior and numerical stability of the iterations, the effectiveness of the low-rank projection, the resolvability of closely spaced angles, as well as the overall computational complexity.

### A. Choice of the step-size

In Algorithm 1, the parameter  $\mu_1$  governs the step-size of the proximal-gradient update and hence directly impacts

---

### Algorithm 2: FRI-based DOA estimation for element-wise nonuniform STAR-RIS

---

```

INPUT:  $\mathbf{y}, N, T_s, K, \alpha, \mu_2, I_{\max}, \varepsilon$ 
OUTPUT:  $\hat{\theta}_1, \dots, \hat{\theta}_K$ 
Initialize  $\boldsymbol{\beta}^{(0)}$ 
for  $i = 1, 2, \dots, I_{\max}$  do
     $\Delta \boldsymbol{\beta}^{(i)} \leftarrow \boldsymbol{\beta}^{(i)} + 2 \mu_2 \boldsymbol{\Psi}^* (\mathbf{y} - \boldsymbol{\Psi}^T \boldsymbol{\beta}^{(i)})$ 
     $\boldsymbol{\beta}^{(i+1)} \leftarrow \Pi_{\mathcal{H}_\alpha^{\text{pair}}}^{-1} (\Pi_{\mathcal{H}_\alpha^{\text{pair}}} (\Pi_{\mathcal{R}_K} (\mathbf{H}_\alpha^{\text{pair}}(\Delta \boldsymbol{\beta}^{(i)}))))$ 
    if  $\|\boldsymbol{\beta}^{(i)} - \boldsymbol{\beta}^{(i+1)}\| \leq \varepsilon$  then  $\hat{\mathbf{x}} = \boldsymbol{\beta}^{(i+1)}$  break
    else
         $\hat{\mathbf{x}} = \boldsymbol{\beta}^{(i+1)}$ 
         $i = i + 1$ 
    end for  $i$ 
 $\mathbf{U}_i, \mathbf{S}_i, \mathbf{V}_i \leftarrow \text{SVD}(\mathbf{H}_\alpha(\hat{\mathbf{x}}_i))$  for  $i \in \{T, R\}$ 
 $\hat{C}_i(z) \leftarrow \hat{\mathbf{c}}_i = \mathbf{V}_i(:, \alpha + 1)$  for  $i \in \{T, R\}$ 
Keep the  $K_R$  roots  $\{\hat{z}_k\}_{k \in \mathcal{K}_R}$  of  $\hat{C}_R(z)$  and the  $K_T$  roots  $\{\hat{z}_k\}_{k \in \mathcal{K}_T}$  of  $\hat{C}_T(z)$  closest to unit circle
 $\hat{\theta}_k = -\arcsin(\arg(\hat{z}_k)/\pi)$  for  $k \in \{1, 2, \dots, K\}$ 

```

---

whether the alternating-projections approximation yields an effective descent direction. The step-size  $\mu_1$  is required to satisfy the condition

$$\frac{1}{2 \lambda_{\max}} \left( 1 - \frac{1}{\sqrt{\alpha + 1}} \right) < \mu_1 < \frac{1}{2 \lambda_{\max}} \left( 1 + \frac{1}{\sqrt{\alpha + 1}} \right) \quad (41)$$

where  $\lambda_{\max} = \sigma_{\max}^2(\boldsymbol{\Phi})$  denotes the largest eigenvalue of  $\boldsymbol{\Phi}^H \boldsymbol{\Phi}$ . The proof is provided in Appendix B. By the same contraction argument used for (41), a similar sufficient condition on the PGD step-size  $\mu_2$  of Algorithm 2 can be derived by replacing  $\lambda_{\max} = \sigma_{\max}^2(\boldsymbol{\Phi})$  with  $\mu_{\max} = \sigma_{\max}^2(\boldsymbol{\Psi})$ , where  $\boldsymbol{\Psi}$  is the sensing matrix defined in (36) for the element-wise nonuniform ES regime.

### B. Choiche of the lifting parameter $\alpha$

The parameter  $\alpha$  controls the dimension of the lifted Hankel-based matrices, thereby influencing both the convergence efficiency of the structured denoising step and the maximum number of resolvable sources. The feasibility condition on  $\alpha$  differs for the two algorithms because the rank constraint is imposed on different lifted objects.

In Algorithm 1, the FRI model order is encoded in each slot-wise Hankel block  $\mathbf{H}_\alpha(\mathbf{b}(t))$  and vertical stacking only increases the number of rows (i.e., the number of equations) without enlarging the column dimension. Hence, the admissible  $\alpha$  is governed by the dimensions of a single Hankel block. Under the low-rank constraint  $\text{rank}(\mathbf{H}_\alpha(\mathbf{b}(t))) \leq K$ , the matrix  $\mathbf{H}_\alpha(\mathbf{b}(t)) \in \mathbb{C}^{(N-\alpha) \times (\alpha+1)}$  admits a non-trivial null space whose dimension is at least

$$\dim \ker(\mathbf{H}_\alpha(\mathbf{b}(t))) \geq (\alpha + 1) - K, \quad (42)$$

provided that  $\alpha \geq K$ . Consequently, the AF coefficients are generally non-unique: there exist  $(\alpha + 1 - K)$  linearly independent null-space vectors. Each null-space vector  $\mathbf{u}$  induces a complex polynomial whose roots necessarily include

$\{e^{-j\pi \sin \theta_k}\}_{k=1}^K$ , thereby enabling parameter recovery via root finding. A larger null-space dimension (i.e., larger  $\alpha$  and/or smaller effective rank) typically improves noise robustness of the denoising, since more redundant algebraic constraints are available. On the other hand, the rank- $K$  truncation is physically meaningful only when the lifted matrix has sufficient degrees of freedom in both dimensions, thus requiring

$$K \leq \min\{\alpha + 1, N - \alpha\}. \quad (43)$$

To guarantee a desired resolvability, we adopt the typical choice  $\alpha = \alpha_1 \triangleq \lfloor \frac{N}{2} \rfloor$  for Algorithm 1.

In Algorithm 2, the low-rank prior is enforced directly on the paired lifting  $\mathbf{H}_\alpha^{\text{pair}}(\boldsymbol{\beta}) = [\mathbf{H}_\alpha(\boldsymbol{\beta}_R), \mathbf{H}_\alpha(\boldsymbol{\beta}_T)]$ , whose column dimension doubles, so the corresponding choice for  $\alpha$  follows from the overall paired matrix dimensions. In this case, the condition becomes

$$K \leq \min\{2(\alpha + 1), N - \alpha\}. \quad (44)$$

We set  $\alpha = \alpha_2 \triangleq \lfloor \frac{N}{3} \rfloor$  for Algorithm 2.

We anticipate that Algorithm 2 has superior performance compared to Algorithm 1. This stems from the enlarged lifting in  $\mathbf{H}_\alpha^{\text{pair}}(\cdot)$ , whose column dimension is  $2(\alpha + 1)$  rather than  $(\alpha + 1)$ . Consequently, the admissible model order is governed by (44) instead of (43), which allows a higher admissible (and thus potentially resolvable) order for a fixed aperture size.

### C. Computational complexity

The computational cost of both methods is dominated by the projection onto the rank- $K$  set, which is implemented via truncated SVD. By comparison, the gradient step and the Hankelization/inverse Hankelization operations (anti-diagonal averaging) require only matrix-vector and blockwise averaging operations and thus incur lower-order complexity (approximately  $\mathcal{O}(T_s N^2)$  per iteration), which is typically smaller than the SVD cost for moderate-to-large  $N$ .

For Algorithm 1, the stacked-Hankel lifting leads to an SVD of a matrix of size  $(N - \alpha) T_s \times (\alpha + 1)$ . With the typical choice  $\alpha \approx N/2$ , the truncated SVD scales as  $\mathcal{O}(T_s \lceil \frac{N}{2} \rceil^3)$  per iteration (up to constant factors depending on the truncation strategy and implementation). For Algorithm 2, the paired lifting produces a larger matrix with column dimension  $2(\alpha + 1)$ . Under  $\alpha \approx N/3$ , the resulting SVD is approximately performed on a near-square matrix of size  $\lceil 2N/3 \rceil \times \lceil 2N/3 \rceil$ , yielding a per-iteration cost on the order of  $\mathcal{O}(\lceil \frac{2N}{3} \rceil^3)$ .

In the large-array regime, the cubic dependence on  $N$  dominates the overall runtime growth, whereas the linear scaling with  $T_s$  has a comparatively milder impact. Accordingly, Algorithm 2 supports a higher admissible model order through its enlarged lifting, at the expense of a higher per-iteration computational cost, which is consistent with the timing results reported in Section V. In practice, both methods converge in a limited number of iterations, keeping the overall computational burden moderate.

### D. Ziv-Zakai bound

This section derives the ZZB for multi-angle estimation in a STAR-RIS-assisted system, following the global tight ZZB framework in [49]. To address the intrinsic permutation ambiguity in multi-target estimation, we adopt the symmetric *mean-squared error* (MSE) metric and obtain a bound expressed as a weighted combination of an a priori bound (APB) and a Cramér–Rao-type term. Specifically, the MSE satisfies

$$\text{MSE} \geq 2P_L \frac{K\zeta^2}{(K+1)^2(K+2)} + \Gamma_{\frac{3}{2}}(\tilde{u}) \frac{\text{Tr}\{\mathbf{F}^{-1}\}}{K} \quad (45)$$

where  $\zeta$  denotes the angular search range,  $\mathbf{F}$  is the Fisher information matrix (FIM),  $P_L$  and  $\tilde{u}$  are given in [49] as

$$P_L = \exp\left(K T_s \left[ \ln\left(\frac{4(1+N\eta)}{(2+N\eta)^2}\right) + \left(\frac{N\eta}{2+N\eta}\right)^2 \right]\right) \cdot \mathcal{Q}\left(\sqrt{2K T_s} \frac{N\eta}{2+N\eta}\right) \quad (46)$$

with  $\mathcal{Q}(\cdot)$  denoting the complementary cumulative distribution function of a standard normal random variable,  $\eta$  representing the per-user signal-to-noise ratio (SNR), and

$$\tilde{u} \approx \min\left\{K T_s \left(\frac{N\eta}{2+N\eta}\right)^2, \frac{K^2 \zeta^2}{8 \mathbf{1}_K^\text{T} \mathbf{F}^{-1} \mathbf{1}_K}\right\}. \quad (47)$$

In typical operating regimes,  $\tilde{u}$  can be further approximated by the first term in (47), i.e., we may write

$$\tilde{u} \approx K T_s \left(\frac{N\eta}{2+N\eta}\right)^2. \quad (48)$$

Here,  $\Gamma_{\frac{3}{2}}(\cdot)$  follows the definition in [49] and acts as a smooth transition weight: at low SNR, the bound is dominated by the APB term, whereas at high SNR it asymptotically approaches the Cramér–Rao bound (CRB) term.

Due to the full-space partitioning of STAR-RIS, the received signals can be decomposed into two subspaces, namely reflection and transmission. For each subspace  $i \in \{\text{R}, \text{T}\}$ , the corresponding FIM is obtained from the derivatives of the steering vectors as

$$\mathbf{F}_i = \frac{2}{T\sigma_n^2} \text{Re}(\mathbf{\Psi}_i^\text{H} \mathbf{\Psi}_i) \quad \text{and} \quad \mathbf{\Psi}_i = \mathbf{\Phi}_i \dot{\mathbf{A}}(\theta_i) \mathbf{s}_i \quad (49)$$

where  $\sigma_n^2$  is the noise variance,  $\mathbf{\Phi}_i$  denotes the (virtual-link) sensing/measurement operator of subspace  $i$ , and

$$\dot{\mathbf{A}}(\theta_i) \triangleq [\dot{\mathbf{a}}(\theta_{i,1}), \dots, \dot{\mathbf{a}}(\theta_{i,K_i})], \quad \dot{\mathbf{a}}(\theta) \triangleq \frac{\partial \mathbf{a}(\theta)}{\partial \theta}. \quad (50)$$

Assuming that the reflection and transmission components are statistically independent and are processed under the same distribution criterion, the ZZB can be evaluated separately in each subspace, thus yielding

$$\text{MSE}_i \geq 2P_L \frac{K_i \zeta^2}{(K_i + 1)^2(K_i + 2)} + \Gamma_{\frac{3}{2}}(\tilde{u}) \frac{\text{Tr}\{\mathbf{F}_i^{-1}\}}{K_i}. \quad (51)$$

Accordingly, a full-space performance lower bound can be defined by aggregating the two subspaces as

$$\text{MSE}_{\text{full}} \triangleq \frac{K_{\text{R}} \text{MSE}_{\text{R}} + K_{\text{T}} \text{MSE}_{\text{T}}}{K_{\text{R}} + K_{\text{T}}} \quad (52)$$

which reduces to  $\text{MSE}_{\text{full}} = (\text{MSE}_{\text{R}} + \text{MSE}_{\text{T}})/2$  when  $K_{\text{R}} = K_{\text{T}}$ . The bound (52) provides a fundamental performance limit for STAR-RIS full-space angle estimation.

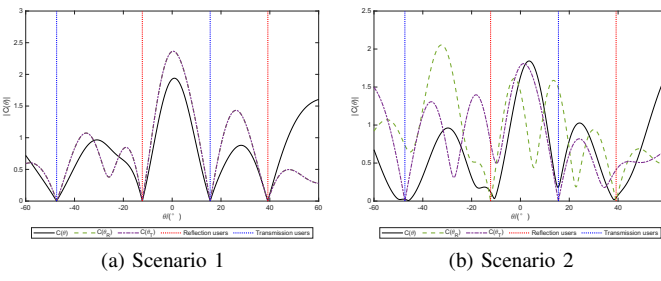


Fig. 2. Spectrum of the AF equations under different scenarios.

## VI. NUMERICAL RESULTS

This section assesses the feasibility, robustness, and angle-estimation accuracy of the proposed methods through numerical simulations. We consider a STAR-RIS-assisted uplink with half-wavelength ULA having  $N = 16$  elements, where all users transmit narrowband signals over the same carrier frequency. Unless otherwise stated, we set  $K = 4$  users with identical SNR, with two users located in the RS and two in the TS. We investigate two STAR-RIS settings: *Scenario 1* (uniform parameters), where  $\beta_{R,n} = \beta_{T,n} = \sqrt{2}/2$  for all  $n$ ; and *Scenario 2* (nonuniform parameters), where  $\beta_{R,n}^2$  is uniformly distributed in  $[0.2, 0.8]$ , subject to (2), and  $\beta_{T,n}$  is determined accordingly. Moreover, to keep the figure legends concise, we adopt abbreviated labels. Specifically, “M1, Scen. 1” refers to the proposed Method 1 evaluated under Scenario 1.

### A. Experiment 1: AF spectrum and root validation

To validate the recovered AF solutions and the corresponding polynomial roots, we adopt the semi-space angle representation. The RS angles are set to  $\theta_R = [-12.23^\circ, 39.19^\circ]$  and the TS angles to  $\theta_T = [-47.34^\circ, 15.57^\circ]$ , with SNR = 15 dB. We scan  $\theta \in [-60^\circ, 60^\circ]$  and plot the AF spectra:  $C(\theta)$  corresponds to Algorithm 1, whereas  $\{C(\theta_R), C(\theta_T)\}$  correspond to the RS/TS subspace equations in Algorithm 2.

Figs. 2a and 2b show that, in Scenario 1, all spectra exhibit pronounced nulls at the true angles. Moreover,  $C(\theta_R) \approx C(\theta_T)$ , which is consistent with the induced rank-one mapping in the uniform-parameter regime: the reconstructed RS/TS submatrices are highly correlated and therefore yield nearly identical null spaces. In Scenario 2, this rank-one coupling is violated. As a result, the single-equation spectrum  $C(\theta)$  produced by Algorithm 1 no longer attains exact zeros and its minima become biased, whereas Algorithm 2 maintains accurate nulls by explicitly enforcing the two subspace AF constraints.

As illustrated in Fig. 3, the AF polynomial typically yields more roots than the number of sources; spurious candidates are removed by enforcing the unit-circle constraint. Under Scenario 2, Algorithm 1 fails to preserve the correct root locations, while Algorithm 1 consistently retains the roots associated with the true angles.

### B. Experiment 2: Estimation accuracy and success probability

We evaluate the full-space angle estimation capability of the proposed approaches, focusing on the angular region in which

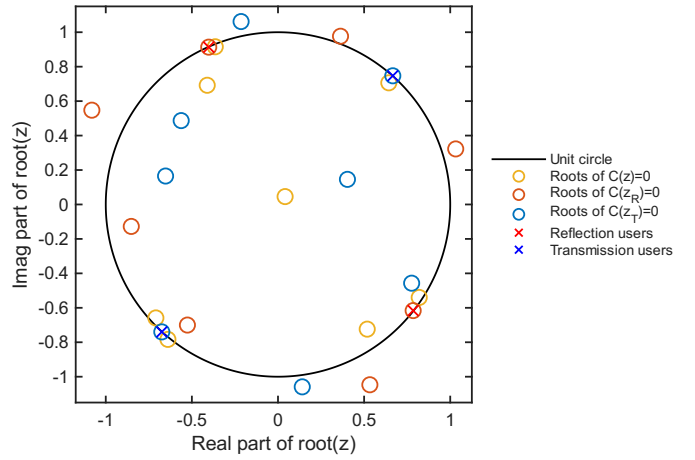


Fig. 3. Root distribution of AF equations (Scenario 2).

reliable estimation is attainable. The full-space representation is adopted throughout. Performance is quantified in terms of (i) estimation accuracy and (ii) success probability. A trial is declared successful if the maximum absolute error satisfies  $\max_k |\hat{\theta}_k - \theta_k| \leq 5^\circ$ , and the success probability is defined as  $p = L_s/L$ , where  $L_s$  denotes the number of successful runs among  $L$  Monte Carlo trials. The accuracy metric is the RMSE computed over successful trials only:

$$\text{RMSE} = \sqrt{\frac{1}{KL_s} \sum_{l=1}^{L_s} \sum_{k=1}^K \left( \hat{\theta}_{k,l} - \theta_k \right)^2}. \quad (53)$$

We consider a two-user setting with one user located in the reflection space and the other in the transmission space. One user’s angle sweeps the full domain with a  $1^\circ$  step, while the other user’s angle is randomly drawn in the opposite space. For each swept angle,  $L = 1000$  Monte Carlo trials are conducted. The resulting RMSE and success-probability curves are reported in Fig. 4 (M1 and M2 stand for Method 1 and Method 2, respectively). As shown in Fig. 4a, both Algorithm 1 and Algorithm 2 exhibit pronounced performance degradation as the impinging direction approaches the coplanar (grazing) case, which is consistent with classical array-based DOA behavior. Fig. 4b further indicates that within  $[-80^\circ, 80^\circ]$  (semi-space representation), the proposed algorithms maintain near-unity success probability and achieve an accuracy on the order of  $0.1^\circ$ . Overall, the results confirm the feasibility of full-space estimation in STAR-RIS systems. To ensure consistently high success probability, we restrict user angles to  $[-60^\circ, 60^\circ]$  (semi-space representation) in the subsequent experiments.

### C. Experiment 3: Convergence behavior

Convergence within a finite number of iterations is essential for both reliability and computational efficiency. Lack of convergence indicates that the PGD iterates do not approach a stationary point, whereas slow convergence translates into excessive runtime. This experiment investigates whether the proposed step-size condition in (41) leads to stable and rapid convergence. Figure 5 depicts the averaged convergence behavior over 1000 Monte Carlo trials. The stopping tolerance is

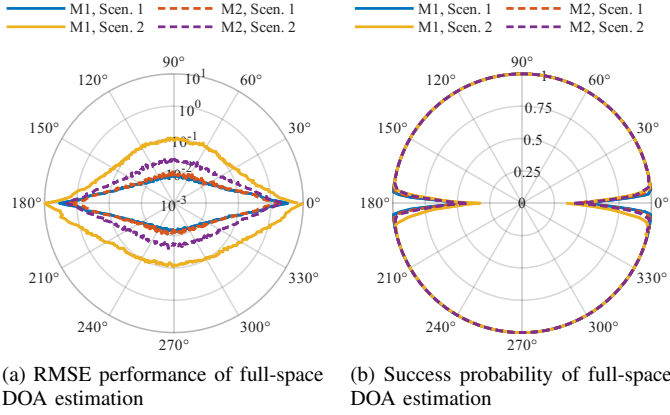


Fig. 4. Evaluation of full-space DOA estimation performance.

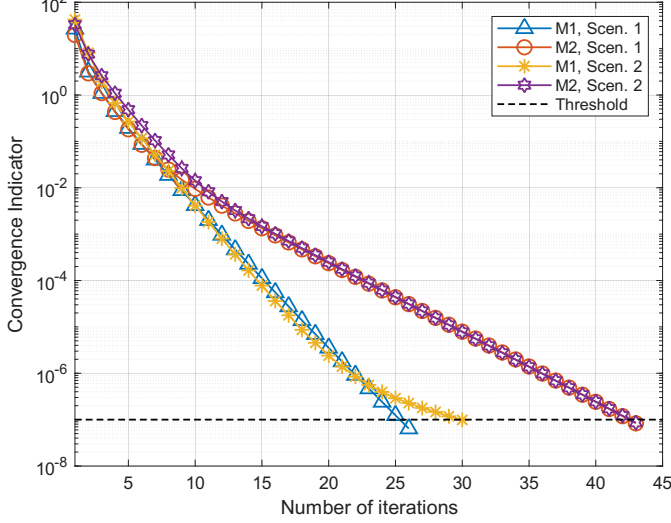


Fig. 5. Convergence behaviors of the proposed algorithms.

set to  $\varepsilon = 10^{-7}$ , and the step-sizes are selected strictly within the admissible interval in (41).

Both Algorithm 1 and Algorithm 2 converge within 45 iterations, and the error decreases to the order of  $10^{-5}$  within approximately 30 iterations. In Scenario 1, the two algorithms exhibit nearly identical exponential decay during the first 20 iterations. Afterwards, Algorithm 1 continues a steady descent and reaches the stopping threshold earlier, whereas Algorithm 2 shows a slower tail. This behavior is mainly due to the joint block-matrix reconstruction in Algorithm 2: as the iterates approach the structured low-rank manifold, the remaining residual becomes dominated by weak noise components, for which the rank- $K$  truncation on the concatenated block matrix yields smaller incremental reductions.

In Scenario 2, the two algorithms follow similar convergence trajectories. However, convergence in this regime only indicates that the PGD iterations have reached an approximate stationary point of the adopted model; the mismatch induced by nonuniform STAR-RIS coefficients may still bias the recovered AF solutions. Overall, these results confirm the practical viability of the proposed solvers and show that the prescribed step-size selection provides stable convergence.

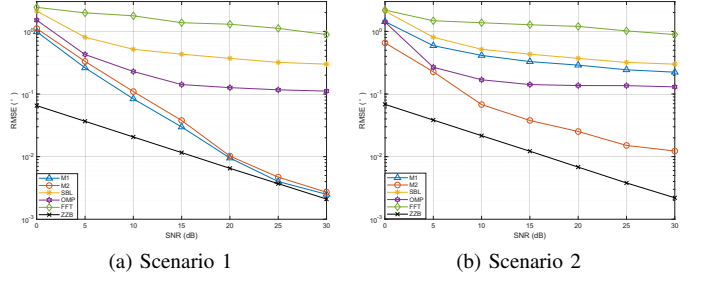


Fig. 6. RMSE versus SNR under different scenarios.

TABLE I  
RUNNING TIME OF DIFFERENT METHODS.

Method	Scenario 1	Scenario 2
FFT	$8.9 \times 10^{-3}$ s	$9.1 \times 10^{-3}$ s
OMP	$7.4 \times 10^{-3}$ s	$8.3 \times 10^{-3}$ s
SBL	$3.2 \times 10^{-2}$ s	$4.3 \times 10^{-2}$ s
Method 1	$8.1 \times 10^{-3}$ s	$8.9 \times 10^{-3}$ s
Method 2	$1.4 \times 10^{-2}$ s	$2.4 \times 10^{-2}$ s

#### D. Experiment 4: RMSE versus SNR

We compare the proposed approaches with three representative baselines: FFT-based beam scanning, orthogonal matching pursuit (OMP), and sparse Bayesian learning (SBL). All baselines estimate the angles in the RS and TS separately. To assess noise robustness, we sweep the SNR from 0 dB to 30 dB in 5 dB increments. The resulting RMSE curves under Scenario 1 and Scenario 2 are reported in Fig. 6.

As shown in Fig. 6a, under Scenario 1 both Algorithm 1 and Algorithm 2 exhibit nearly identical trends and consistently outperform FFT/OMP/SBL over the entire SNR range. In the high-SNR regime, their RMSE approaches the ZZB, indicating that the proposed gridless formulations mitigate the resolution loss and grid mismatch that limit discretized methods.

Under Scenario 2 (see Fig. 6b), Algorithm 1 experiences a marked degradation because the rank-one coupling assumed in the uniform-parameter model is violated. Consequently, a single AF relation is generally insufficient to yield unbiased root estimates. In contrast, Algorithm 2 remains robust by explicitly exploiting the two-subspace structure and preserves a clear advantage over all baselines. Compared with Scenario 1, its RMSE increases moderately, as element-wise amplitude variations effectively reduce the useful aperture (and the effective SNR), which in turn degrades accuracy.

#### E. Experiment 5: Computational cost

This experiment benchmarks the computational efficiency of the proposed algorithms against the FFT-, OMP-, and SBL-based baselines. Table I reports the average runtime per Monte Carlo run (in seconds) measured in MATLAB, for both Scenario 1 and Scenario 2.

As shown in Table I, FFT- and OMP-based methods exhibit the lowest runtime due to their lightweight grid-based processing. Algorithm 1 attains a runtime of the same order, indicating that the structured PGD-AP solver incurs only limited additional overhead. Algorithm 2 is more computationally

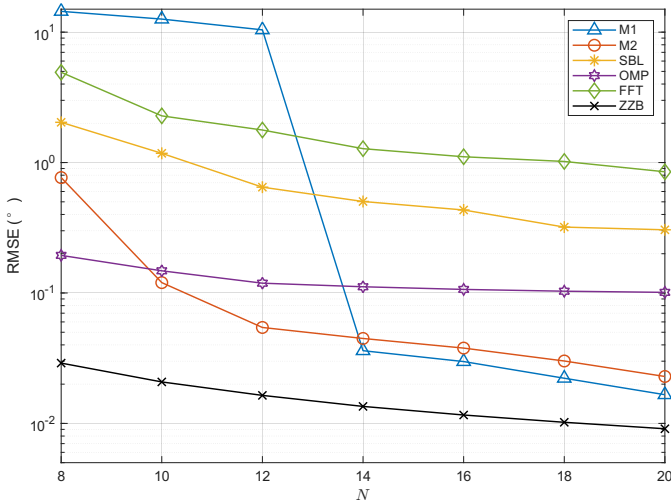


Fig. 7. RMSE versus the number of elements (Scenario 1).

demanding, which is consistent with Experiment 3: it relies on a higher-dimensional lifted (block) matrix and therefore requires a costlier truncated-SVD projection at each iteration. The runtime gap becomes more evident in Scenario 2, where the nonuniform-parameter setting typically leads to slower convergence and/or less favorable numerical conditioning.

#### F. Experiment 6: Effect of STAR-RIS size

This experiment examines the impact of the STAR-RIS aperture on estimation accuracy by varying the number of metasurface elements from  $N = 8$  to  $N = 20$  in steps of 2 under Scenario 1. The corresponding RMSE results are reported in Fig. 7. It can be seen that the proposed algorithms exhibit a stronger dependence on  $N$  than the three baselines. Once a minimum aperture requirement is met (e.g.,  $N > K$ ), FFT/OMP/SBL show only a mild improvement with increasing  $N$ . In contrast, the proposed FRI/Hankel-based solvers benefit directly from a larger lifting dimension, which strengthens the structured low-rank constraint, improves denoising, and stabilizes the subsequent root-extraction step.

For small apertures, Algorithm 1 may approach (or violate) the feasibility limits of the rank- $K$  truncation due to insufficient lifted degrees of freedom, resulting in unstable estimation. As  $N$  increases, its performance improves rapidly and approaches the best attainable accuracy. Algorithm 2 remains applicable over the entire range of  $N$  thanks to the paired formulation, but its RMSE degrades in the small- $N$  regime because reduced Hankel dimensions weaken the effectiveness of the SVD-based noise suppression and make the annihilation-based recovery more sensitive to perturbations.

Overall, results highlight an inherent trade-off of the proposed structured lifting: smaller STAR-RIS apertures limit the effectiveness of the low-rank model, whereas larger apertures enhance denoising capability and angular resolvability.

## VII. CONCLUSION

This paper studied full-space DOA estimation in STAR-RIS-assisted ISAC systems using a FRI formulation. By

exploiting STAR-RIS reflection/transmission coupling, we developed two gridless recovery schemes: an efficient approach tailored to the element-wise uniform regime and a more general method that remains applicable under element-wise nonuniform energy splitting. Both schemes combine structured denoising via a proximal-gradient iteration with alternating projections and subsequent DOA retrieval through annihilating-filter root finding. We further derived the ZZB to benchmark performance limits, and numerical results demonstrate reliable full-space coverage and consistent gains over grid-based baselines, while highlighting degradation near grazing angles and under strong nonuniformity.

## APPENDIX A APPROXIMATE STACKED-HANKEL STRUCTURE AFTER SVD TRUNCATION

Let  $\mathcal{H}_\alpha^{\text{stack}}$  denote the linear subspace of matrices that have the stacked-Hankel structure induced by the lifting operator  $\mathbf{H}_\alpha^{\text{stack}}(\cdot)$ . Given  $\mathbf{Q}_\alpha^{\text{stack}} \in \mathbb{C}^{(N-\alpha)T_s \times (\alpha+1)}$ , Algorithm 1 forms its rank- $K$  truncation via SVD as follows

$$\mathbf{Q}_\alpha^{\text{stack}} = \mathbf{U}\Sigma\mathbf{V}^H \Rightarrow \mathbf{Q}_K^{\text{stack}} \triangleq \mathbf{U}\Sigma_K\mathbf{V}^H \quad (54)$$

where  $\Sigma_K$  retains only the  $K$  largest singular values. Since the set  $\mathcal{H}_\alpha^{\text{stack}}$  is independent of the rank constraint, the matrix  $\mathbf{Q}_K^{\text{stack}}$  is not guaranteed to be stacked Hankel. Nevertheless, under the FRI generative model it is *approximately* stacked Hankel, in the sense that its distance to  $\mathcal{H}_\alpha^{\text{stack}}$  is small.

To show this, let us assume that  $\mathbf{Q}_\alpha^{\text{stack}}$  can be written as

$$\mathbf{Q}_\alpha^{\text{stack}} = \mathbf{H}^{\text{stack}} + \mathbf{E}, \quad (55)$$

where  $\mathbf{H}^{\text{stack}} \in \mathcal{H}_\alpha^{\text{stack}}$  is an *ideal* stacked-Hankel matrix generated by a  $K$ -sparse line-spectrum sequence, and  $\mathbf{E}$  collects noise and modeling errors, whose entries are independent and identically distributed (i.i.d.) zero-mean complex circular Gaussian variables with variance  $\sigma_e^2$ . In particular, the FRI property implies that  $\text{rank}(\mathbf{H}^{\text{stack}}) \leq K$ . Let  $\text{dist}(\mathbf{X}, \mathcal{H}_\alpha^{\text{stack}}) \triangleq \min_{\mathbf{Z} \in \mathcal{H}_\alpha^{\text{stack}}} \|\mathbf{X} - \mathbf{Z}\|_F$  be the Frobenius distance to the stacked-Hankel subspace. We have

$$\begin{aligned} \text{dist}(\mathbf{Q}_K^{\text{stack}}, \mathcal{H}_\alpha^{\text{stack}}) &\leq \|\mathbf{Q}_K^{\text{stack}} - \mathbf{H}^{\text{stack}}\|_F \\ &\leq \|\mathbf{Q}_K^{\text{stack}} - \mathbf{Q}_\alpha^{\text{stack}}\|_F + \|\mathbf{E}\|_F. \end{aligned} \quad (56)$$

By virtue of the Eckart–Young’s theorem [50], the first term in (56) is controlled by

$$\|\mathbf{Q}^{\text{stack}} - \mathbf{Q}_K^{\text{stack}}\|_F^2 = \sum_{i>K} \sigma_i^2(\mathbf{Q}^{\text{stack}}). \quad (57)$$

Moreover, by Weyl’s inequality [47], one gets

$$\sigma_{K+1}(\mathbf{Q}^{\text{stack}}) \leq \sigma_{K+1}(\mathbf{H}^{\text{stack}}) + \|\mathbf{E}\|_2 = \|\mathbf{E}\|_2, \quad (58)$$

because  $\sigma_{K+1}(\mathbf{H}^{\text{stack}}) = 0$  when  $\text{rank}(\mathbf{H}^{\text{stack}}) \leq K$ , and  $\|\mathbf{E}\|_2$  is the spectral norm of  $\mathbf{E}$ . Hence, it follows that

$$\|\mathbf{Q}_\alpha^{\text{stack}} - \mathbf{Q}_K^{\text{stack}}\|_F \leq \|\mathbf{Q}_\alpha^{\text{stack}} - \mathbf{H}^{\text{stack}}\|_F = \|\mathbf{E}\|_F \quad (59)$$

$$\begin{aligned} \text{dist}(\mathbf{Q}_K^{\text{stack}}, \mathcal{H}_\alpha^{\text{stack}}) &\leq \|\mathbf{Q}_K^{\text{stack}} - \mathbf{H}^{\text{stack}}\|_F \\ &\leq \|\mathbf{Q}_K^{\text{stack}} - \mathbf{Q}_\alpha^{\text{stack}}\|_F + \|\mathbf{E}\|_F \\ &\leq 2\|\mathbf{E}\|_F. \end{aligned} \quad (60)$$

Therefore, the rank- $K$  SVD truncation  $\mathbf{Q}_K^{\text{stack}}$  is guaranteed to lie in a small neighborhood of the stacked-Hankel subspace whenever  $\|\mathbf{E}\|_F$  is small. In particular, each stacked block is also close to the Hankel set in the same Frobenius sense.

Since the noise is modeled as circularly symmetric complex Gaussian, the squared Frobenius norm  $\|\mathbf{E}\|_F^2$  (after normalization by  $\sigma_e^2$ ) follows a chi-square distribution with degrees of freedom proportional to the number of complex entries. We therefore invoke the standard Laurent-Massart concentration inequality for chi-square random variables [51], thus yielding

$$\mathbb{P}\left(\|\mathbf{E}\|_F \leq \sigma_e \left[\sqrt{M} + \sqrt{2 \ln(\delta^{-1})}\right]\right) \geq 1 - \delta \quad (61)$$

with  $M \triangleq (N - \alpha)T_s(\alpha + 1)$ , for any  $\delta \in (0, 1)$ . Thus, we can conclude that

$$\|\mathbf{E}\|_F \leq \sigma_e \left[\sqrt{M} + \sqrt{2 \ln(\delta^{-1})}\right] \quad (62)$$

with probability at least  $1 - \delta$ . In particular, since  $\mathbf{H}^{\text{stack}}$  is formed by vertically stacking Hankel sub-blocks, the above bound immediately implies that each reconstructed sub-block of  $\mathbf{Q}_K^{\text{stack}}$  is itself close to the Hankel set  $\mathcal{H}_\alpha$ . More precisely, if  $\mathbf{Q}_K^{\text{stack}} = [\mathbf{Q}_{K,1}^T, \dots, \mathbf{Q}_{K,T_s}^T]^T$ , then

$$\text{dist}(\mathbf{Q}_{K,t}, \mathcal{H}_\alpha) \leq \text{dist}(\mathbf{Q}_K^{\text{stack}}, \mathcal{H}_\alpha^{\text{stack}}) \quad (63)$$

for all  $t \in \mathcal{T}$ , i.e., every slot-wise sub-block preserves an approximately Hankel structure.

## APPENDIX B PROOF OF THE STEP-SIZE CONDITION

We establish a sufficient condition on the PGD step-size for Algorithm 1 by showing that the update based on alternating projections (AP) defines a contraction mapping. Algorithm 2 follows by applying the same argument to the corresponding block operator. Let us define the gradient step associated with the quadratic data-fidelity term as

$$P_{\mu_1}(\mathbf{a}) \triangleq \mathbf{a} + 2\mu_1 \Phi^H (\mathbf{y} - \Phi \mathbf{a}) \quad (64)$$

and define the AP-induced update as

$$U_{\mu_1}(\mathbf{a}) \triangleq \Pi_{\mathcal{H}_\alpha^{\text{stack}}}^{-1} \left( \Pi_{\mathcal{H}_\alpha^{\text{stack}}} \left( \Pi_{\mathcal{R}_K} \left( \mathbf{H}_\alpha^{\text{stack}}(\mathbf{a}) \right) \right) \right). \quad (65)$$

Since  $\Phi^H \Phi$  is a positive definite Hermitian matrix [47], for any  $\mathbf{a}_1, \mathbf{a}_2 \in \mathbb{C}^{NT_s}$  we have

$$\begin{aligned} \|P_{\mu_1}(\mathbf{a}_1) - P_{\mu_1}(\mathbf{a}_2)\|_2 &= \|(\mathbf{I}_{NT_s} - 2\mu_1 \Phi^H \Phi)(\mathbf{a}_1 - \mathbf{a}_2)\|_2 \\ &\leq \rho_{\mu_1} \|\mathbf{a}_1 - \mathbf{a}_2\|_2 \end{aligned} \quad (66)$$

where the spectral norm

$$\begin{aligned} \rho_{\mu_1} &\triangleq \|\mathbf{I}_{NT_s} - 2\mu_1 \Phi^H \Phi\|_2 \\ &= \max \{|1 - 2\mu_1 \lambda_{\min}|, |1 - 2\mu_1 \lambda_{\max}|\} \end{aligned} \quad (67)$$

with  $\lambda_{\min}$  and  $\lambda_{\max}$  being the extreme eigenvalues of  $\Phi^H \Phi$ .

Next, the Hankel lifting satisfies

$$\|\mathbf{H}_\alpha^{\text{stack}}(\mathbf{a}_1) - \mathbf{H}_\alpha^{\text{stack}}(\mathbf{a}_2)\|_F \leq \sqrt{\alpha + 1} \|\mathbf{a}_1 - \mathbf{a}_2\|_2 \quad (68)$$

because each entry of  $\mathbf{a}_1 - \mathbf{a}_2$  appears at most  $(\alpha + 1)$  times in  $\mathbf{H}_\alpha^{\text{stack}}(\cdot)$ , and hence the Frobenius norm aggregates at most

$(\alpha + 1)$  copies of each squared magnitude. Moreover, the rank- $K$  truncation is non-expansive in Frobenius norm, that is,

$$\|\Pi_{\mathcal{R}_K}(\mathbf{A}_1) - \Pi_{\mathcal{R}_K}(\mathbf{A}_2)\|_F \leq \|\mathbf{A}_1 - \mathbf{A}_2\|_F. \quad (69)$$

Finally, inverse Hankelization (anti-diagonal averaging) is non-expansive from Frobenius to Euclidean norm:

$$\left\| \Pi_{\mathcal{H}_\alpha^{\text{stack}}}^{-1}(\mathbf{A}_1) - \Pi_{\mathcal{H}_\alpha^{\text{stack}}}^{-1}(\mathbf{A}_2) \right\|_2 \leq \|\mathbf{A}_1 - \mathbf{A}_2\|_F. \quad (70)$$

Combining (66)–(70) yields

$$\|U_{\mu_1}(\mathbf{a}_1) - U_{\mu_1}(\mathbf{a}_2)\|_2 \leq \sqrt{\alpha + 1} \rho_{\mu_1} \|\mathbf{a}_1 - \mathbf{a}_2\|_2. \quad (71)$$

Therefore, if  $\sqrt{\alpha + 1} \rho_{\mu_1} < 1$ , the mapping  $U_{\mu_1}$  is a contraction and admits a unique fixed point. By the Banach fixed-point theorem [52], the fixed-point iteration  $\mathbf{a}^{(i+1)} = U_{\mu_1}(\mathbf{a}^{(i)})$  converges linearly to this point. A sufficient condition for  $\rho_{\mu_1} \leq 1/\sqrt{\alpha + 1}$  is obtained by requiring that inequalities  $|1 - 2\mu_1 \lambda_{\min}| \leq 1/\sqrt{\alpha + 1}$  and  $|1 - 2\mu_1 \lambda_{\max}| \leq 1/\sqrt{\alpha + 1}$  hold. A simple (conservative) bound is obtained using  $\lambda_{\max}$  only, which yields (41).

## REFERENCES

- [1] S. Lyu, X. Hu, C. Liu, and M. Peng, “IRS-aided location sensing and beamforming in ISAC systems: Distributed or not?,” *IEEE Trans. Veh. Technol.*, vol. 73, no. 9, pp. 13219–13233, Sep. 2024.
- [2] Z. Yu, X. Hu, C. Liu, M. Peng, and C. Zhong, “Location sensing and beamforming design for IRS-enabled multi-user ISAC systems,” *IEEE Trans. Signal Process.*, vol. 70, pp. 5178–5193, 2022.
- [3] K. Xu, X. Xia, C. Li, G. Hu, Q. Su, and W. Xie, “Spatial structure matching-based DOA estimation and tracking for integrated sensing and communication massive MIMO OFDM system,” *IEEE Trans. Cogn. Commun. Netw.*, vol. 10, no. 2, pp. 526–540, 2023.
- [4] K. Xu, X. Xia, C. Li, C. Wei, W. Xie, and Y. Shi, “Channel feature projection clustering based joint channel and DOA estimation for ISAC massive MIMO OFDM system,” *IEEE Trans. Veh. Technol.*, vol. 73, no. 3, pp. 3678–3689, 2023.
- [5] C. Yu, Y. Li, L. Li, Z. Huang, Q. Wu, and R. de Lamare, “Dual Lawson norm-based robust DOA estimation for RIS-aided wireless communication systems,” *IEEE Trans. Aerosp. Electron. Syst.*, vol. 61, no. 1, pp. 582–592, 2024.
- [6] L. Boccia, I. Russo, G. Amendola, and G. Di Massa, “Multilayer antenna-filter antenna for beam-steering transmit-array applications,” *IEEE Trans. Microw. Theory Techn.*, vol. 60, no. 7, pp. 2287–2300, Jul. 2012.
- [7] J. Y. Lau and S. V. Hum, “A wideband reconfigurable transmitarray element,” *IEEE Trans. Antennas Propag.*, vol. 60, no. 3, pp. 1303–1311, Mar. 2012.
- [8] R. Liu, M. Li, Q. Liu, and A. L. Swindlehurst, “SNR/CRB-constrained joint beamforming and reflection designs for RIS-ISAC systems,” *IEEE Trans. Wireless Commun.*, vol. 23, no. 7, pp. 7456–7470, 2023.
- [9] D. Wang, Z. Wang, W. Yang, H. Zhao, Y. He, L. Li, Z. Wei, and F. Zhou, “Enhanced ISAC framework for moving target assisted by beyond-diagonal RIS: Accurate localization and efficient communication,” *IEEE Trans. Netw. Sci. Eng.*, vol. 12, no. 5, pp. 4299–4315, Sep.–Oct. 2025.
- [10] A. Megahed, A. M. Abd El-Haleem, M. M. Elmesalawy, *et al.*, “Deep learning optimization of STAR-RIS for enhanced data rate and energy efficiency in 6G wireless networks,” *Sci. Rep.*, 2025.
- [11] X. Ma, Y. Fang, H. Zhang, S. Guo, and D. Yuan, “Cooperative beamforming design for multiple RIS-assisted communication systems,” *IEEE Trans. Wireless Commun.*, vol. 21, no. 12, pp. 10949–10963, Dec. 2022.
- [12] M. Ahmed, A. Wahid, S. S. Laique, W. U. Khan, A. Ihsan, F. Xu, S. Chatzinotas, and Z. Han, “A survey on STAR-RIS: Use cases, recent advances, and future research challenges,” *IEEE Internet Things J.*, vol. 10, no. 16, pp. 14689–14711, 2023.
- [13] X. Mu, Y. Liu, L. Guo, J. Lin, and R. Schober, “Simultaneously transmitting and reflecting (STAR) RIS aided wireless communications,” *IEEE Trans. Wireless Commun.*, vol. 21, no. 5, pp. 3083–3098, May 2021.
- [14] N. Xue, X. Mu, Y. Liu, and Y. Chen, “NOMA-assisted full-space STAR-RIS-ISAC,” *IEEE Trans. Wireless Commun.*, vol. 23, no. 8, pp. 8954–8968, Aug. 2024.

[15] J. Xu, Y. Liu, X. Mu, and O. A. Dobre, "STAR-RISs: Simultaneous transmitting and reflecting reconfigurable intelligent surfaces," *IEEE Commun. Lett.*, vol. 25, no. 9, pp. 3134–3138, Sep. 2021.

[16] F. Verde, V. Galdi, L. Zhang, and T. J. Cui, "Integrating sensing and communications: Simultaneously transmitting and reflecting digital coding metasurfaces - A successful convergence of physics and signal processing," *IEEE Signal Process. Mag.*, vol. 41, no. 5, pp. 56–70, Sep. 2024.

[17] X. Yue, J. Xie, Y. Liu, Z. Han, R. Liu, and Z. Ding, "Simultaneously transmitting and reflecting reconfigurable intelligent surface assisted NOMA networks," *IEEE Trans. Wireless Commun.*, vol. 22, no. 1, pp. 189–204, Jan. 2023.

[18] J. He, A. Fakhreddine, and G. C. Alexandopoulos, "STAR-RIS-enabled simultaneous indoor and outdoor 3D localisation: Theoretical analysis and algorithmic design," *IET Signal Process.*, vol. 17, no. 4, 2023.

[19] J. He, A. Fakhreddine, and G. C. Alexandopoulos, "Simultaneous indoor and outdoor 3D localization with STAR-RIS-assisted millimeter wave systems," in *Proc. IEEE 96th Veh. Technol. Conf. (VTC-Fall)*, London, U.K., 2022, pp. 1–6.

[20] M. Li, S. Zhang, Y. Ge, Z. Li, F. Gao, and P. Fan, "STAR-RIS aided integrated sensing and communication over high-mobility scenario," *IEEE Trans. Commun.*, vol. 72, no. 8, pp. 4788–4802, Aug. 2024.

[21] K. Meng, Q. Wu, W. Chen, and D. Li, "Sensing-assisted communication in vehicular networks with intelligent surface," *IEEE Trans. Veh. Technol.*, vol. 73, no. 1, pp. 876–893, Jan. 2024.

[22] ETSI, *Reconfigurable Intelligent Surfaces (RIS): Multi-functional Reconfigurable Intelligent Surfaces (RIS): Modelling, Optimization, and Operation*, ETSI GR RIS 006, v1.1.1, Jun. 2025.

[23] R. O. Schmidt, "Multiple emitter location and signal parameter estimation," *IEEE Trans. Antennas Propag.*, vol. 34, no. 3, pp. 276–280, Mar. 1986.

[24] R. Roy, A. Paulraj, and T. Kailath, "Estimation of signal parameters via rotational invariance techniques - ESPRIT," in *Proc. MILCOM*, vol. 3, 1986, pp. 41.6.1–41.6.5.

[25] P. Gonnet, S. Güttel, and L. N. Trefethen, "Robust Padé approximation via SVD," *SIAM Rev.*, vol. 55, no. 1, pp. 101–117, 2013.

[26] M. Zuo, S. Xie, X. Zhang, and M. Yang, "DOA estimation based on weighted  $\ell_1$ -norm sparse representation for low-SNR scenarios," *Sensors*, vol. 21, no. 13, Art. no. 4614, 2021.

[27] P. Gerstoft, C. F. Mecklenbräuker, A. Xenaki, and S. Nannuru, "Multisnapshot sparse Bayesian learning for DOA," *IEEE Signal Process. Lett.*, vol. 23, no. 10, pp. 1469–1473, Oct. 2016.

[28] Y. Jin, D. He, S. Wei, and W. Yu, "Off-grid DOA estimation method based on sparse Bayesian learning with clustered structural-aware prior information," *IEEE Trans. Veh. Technol.*, vol. 73, no. 4, pp. 5469–5483, 2023.

[29] M. Lin *et al.*, "Single sensor to estimate DOA with programmable metasurface," *IEEE Internet Things J.*, vol. 8, no. 12, pp. 10187–10197, Jun. 2021.

[30] Z. Wang, W. Yang, T. Mi, and R. Qi, "Joint beamforming design and 3D DoA estimation for RIS-aided communication system," arXiv preprint arXiv:2211.01640, 2022.

[31] R. Chavanne, K. Abed-Meraim, and D. Medynski, "Two-step MUSIC algorithm for improved array resolution," in *Proc. IEEE Statist. Signal Process. Workshop (SSP)*, 2001, pp. 512–515.

[32] P. Chen, Z. Chen, B. Zheng, and X. Wang, "Efficient DOA estimation method for reconfigurable intelligent surfaces aided UAV swarm," *IEEE Trans. Signal Process.*, vol. 70, pp. 743–755, 2022.

[33] Y. Zheng, Q. Wang, L. Ren, Z. Ma, and P. Fan, "RIS-aided gridless 2D-DOA estimation via decoupled atomic norm minimization," *IEEE Trans. Veh. Technol.*, vol. 73, no. 10, pp. 15733–15738, Oct. 2024.

[34] L. Li, C. Yu, Y. Li, Z. Huang, and Q. Wu, "Joint squared-sine function and ANM-based DOA estimation with RIS," *IEEE Trans. Veh. Technol.*, vol. 72, no. 12, pp. 16856–16860, Dec. 2023.

[35] P. Chen, Z. Yang, Z. Chen, and Z. Guo, "Reconfigurable intelligent surface aided sparse DOA estimation method with non-ULA," *IEEE Signal Process. Lett.*, vol. 28, pp. 2023–2027, 2021.

[36] Q. Li, K. Huang, X. Wang, K. Liu, and M. Yi, "Simultaneously transmitting and reflecting reconfigurable intelligent surface assisted full-space direction-of-arrival estimation," in *Proc. Int. Conf. Microw. Millim. Wave Technol. (ICMWT)*, 2024, pp. 1–3.

[37] H. Pan, T. Blu, and M. Vetterli, "Towards generalized FRI sampling with an application to source resolution in radio astronomy," *IEEE Trans. Signal Process.*, vol. 65, no. 4, pp. 821–835, Feb. 2017.

[38] M. Simeoni, A. Besson, P. Hurley, and M. Vetterli, "CPGD: Cadzow plug-and-play gradient descent for generalised FRI," *IEEE Trans. Signal Process.*, vol. 69, pp. 42–57, 2021.

[39] H. Pan, T. Blu, and M. Vetterli, "Efficient multidimensional Diracs estimation with linear sample complexity," *IEEE Trans. Signal Process.*, vol. 66, no. 17, pp. 4642–4656, Sep. 2018.

[40] K. Wang, L. Shi, and T. Chen, "Two-dimensional separable gridless direction-of-arrival estimation based on finite rate of innovation," *IEEE Access*, vol. 9, pp. 17275–17283, 2021.

[41] Y. Li, R. Guo, T. Blu, and H. Zhao, "Generic FRI-based DOA estimation: A model-fitting method," *IEEE Trans. Signal Process.*, vol. 69, pp. 4102–4115, 2021.

[42] H. Pan, R. Scheibler, E. Bezzam, I. Dokmanić, and M. Vetterli, "FRIDA: FRI-based DOA estimation for arbitrary array layouts," in *Proc. IEEE ICASSP*, 2017, pp. 3186–3190.

[43] R. Guo, Y. Li, T. Blu, and H. Zhao, "Vector-FRI recovery of multi-sensor measurements," *IEEE Trans. Signal Process.*, vol. 70, pp. 4369–4380, 2022.

[44] N. Parikh and S. Boyd, "Proximal Algorithms," *Foundations and Trends in Optimization*, vol. 1, no. 3, pp. 127–239, 2014.

[45] A. Beck and M. Teboulle, "A fast iterative shrinkage-thresholding algorithm for linear inverse problems," *SIAM Journal on Imaging Sciences*, vol. 2, no. 1, pp. 183–202, 2009.

[46] F. Andersson and M. Carlsson, "Alternating projections on low-dimensional manifolds," in *Proc. Project Rev.*, vol. 1, 2011, pp. 37–56.

[47] R.A. Horn and C.R. Johnson, *Matrix Analysis*. New York: Cambridge Univ. Press, 1990.

[48] L. Bao, Q. Ma, R.Y. Wu, X. Fu, J. Wu, and T.J. Cui, "Programmable reflection-transmission shared-aperture metasurface for real-time control of electromagnetic waves in full space," *Adv. Sci.*, vol. 8, no. 15, Art no. 2100149, Aug. 2021.

[49] Z. Zhang, Z. Shi, and Y. Gu, "Ziv-Zakai bound for DOA estimation," *IEEE Trans. Signal Process.*, vol. 71, pp. 136–149, 2023.

[50] C. Eckart and G. Young, "The approximation of one matrix by another of lower rank," *Psychometrika*, vol. 1, pp. 211–218, Sep. 1936.

[51] R. Vershynin, *High-Dimensional Probability: An Introduction with Applications in Data Science*. Cambridge, U.K.: Cambridge Univ. Press, 2018.

[52] K. Goebel and W. A. Kirk, *Topics in Metric Fixed Point Theory*. Cambridge, U.K.: Cambridge Univ. Press, 1990.